An Implicit Integral Formulation to Model Inviscid Fluid Flows in Obstructed Media

Clément Colas, Martin Ferrand, Jean-Marc Hérard, Jean-Claude Latché, Erwan Le Coupanec

An Implicit Integral Formulation to Model Inviscid Fluid Flows in Obstructed Media

Clément Colas[a,b], Martin Ferrand[a], Jean-Marc Hérard[a,b], Jean-Claude Latché[b,c], Erwan Le Coupanec[a]

[a] *EDF R&D, MFEE, 6 quai Watier, 78400, Chatou, France*
[b] *Aix-Marseille Université, I2M, UMR CNRS 7373, 39 rue Joliot Curie, 13453, Marseille, France*
[c] *IRSN, Cadarache, 13115, Saint-Paul-Lez-Durance Cedex, France*

Abstract

We focus here on a technique to compute compressible fluid flows in physical domains cluttered up with many small obstacles. This technique, referred to here as the integral formulation, consists in integrating the flow governing equations over the fluid part of control volumes including both fluid and solid zones; doing so, the integral of fluxes over solid boundaries may appear, for which expressions as a function of discrete variables must be provided. The integral formulation presents two essential advantages: first, we naturally recover the standard fluid approach when the mesh is refined; second, fluid/solid interactions may be, to some extent, modelled to recover the singular head losses at the interface between a free and a congested part of the computational domain. We apply here this approach to the Euler equations, using a collocated space discretization and a pressure correction algorithm, preserving the positivity of both the density and the internal energy. Verification test cases are performed, including a Riemann problem in a free domain and a shock wave reflection on a wall, using an equation of state which is suitable for weakly compressible fluid flows. Finally, we address a two-dimensional situation, where a shock wave impacts a set of obstacles; we observe a very encouraging agreement between the integral approach results and a CFD reference solution obtained with a pure fluid approach on a fine mesh.

Keywords: Finite Volumes, integral formulation, porous media, compressible flows, Euler equations, pressure-correction scheme

1. Introduction

The issue of dealing with congested media is pervasive in industrial Computational Fluid Dynamics applications. In the easiest cases, the computational domain (*i.e.*, in practice, the mesh) may be fitted to the boundary of each of the present solids, but in many applications, these latter are too numerous or too small with respect to the computational domain characteristic dimensions to be dealt with in such a way: this would imply using so refined meshes that the computational cost would become prohibitive. In

Email addresses: clement.colas@edf.fr (Clément Colas), martin.ferrand@edf.fr (Martin Ferrand), jean-marc.herard@edf.fr (Jean-Marc Hérard), jean-claude.latche@irsn.fr (Jean-Claude Latché), erwan.lecoupanec@edf.fr (Erwan Le Coupanec)

nuclear industry, occurrences of such problems are numerous. One may think for instance of safety issues as possible cables train fires, hydrogen deflagration in the reactor building rooms where numerous pipes are present... For the computation of the flow in the primary circuit of Pressurized Water Reactors, both in operating and accident conditions [1, 2], the problem has been tackled now for more than forty years, and has motivated the development of, schematically speaking, three categories of simulation software, each acting at its own scale:

- At the largest scale, referred to as the *system* scale, a 0D/1D description is used, with the aim to provide a real time simulation of full circuits (system transient analysis). A reference industrial code in France is CATHARE [3], developed from the end of the 70s thanks to a joint effort by several partners, among which, in particular, CEA (Commissariat à l'Énergie Atomique et aux Énergies Alternatives), EDF and IRSN (Institut de Radioprotection et de Sûreté Nucléaire).

- The finest one is the CFD (Computational Fluid Dynamics) scale, referred to as the *local* scale, that allows a fine 3D description on restricted physical domains. In that case, the Navier-Stokes equations, with suitable turbulence modelling, are solved on fine computational meshes, and all solid boundaries of obstacles in the computational domain are meshed through standard wall boundary conditions. *Code_Saturne* [4] (developed by EDF R&D since 1997) is one of the CFD codes used in this context.

- Since computations at the largest scale may be too crude and application at the local scale are often too time-consuming, an intermediate approach, aiming at the description of one component of the primary circuit such as the reactor core or the steam generator, has been developed; software dedicated to this purpose are said to operate at the *component* scale. In this case, an homogenized representation is chosen: the congested medium is considered as a porous medium, in which three-dimensional balance equations (mass, momentum and energy) are solved; the influence of the solid obstacles is taken into account, besides of course a reduction of the porosity, through exchange terms (a friction term for the momentum balance and a heat exchange term for the energy balance) obtained by upscaling techniques. The component approach is implemented, for instance, in codes developed in the 80s such as THYC [5], FLICA-4 [6] or GENEPI [7, 8, 9].

Enlarging the scope to another already mentioned safety problem, namely turbulent deflagrations, a strategy similar to what is done in thermal-hydraulics at the component scale is employed in the commercial code FLACS [10].

The "equivalent porous media approach", as used in component codes, has now proven to yield accurate results for incompressible or quasi-incompressible flows in porous media where a micro-scale and a representative elementary volume associated to this scale may be identified [11] (so, in particular, for periodic media). Its extension to compressible flows is however less standard and, in addition, serious difficulties may appear when the characteristics of the equivalent porous medium sharply vary with space. In particular, the numerical study [12] shows that the porous model is not physically suitable to manage sudden free/porous transitions: the comparison between the multi-dimensional CFD computation, including the true geometry of obstacles (as shown on Figure 1), and

the equivalent porous computation (see Figure 2) shows discrepancies at the interface associated with the discontinuity in the equivalent porosity profile. These discrepancies may be attributed to the fact that the singular head loss in the momentum balance is not accounted for in the porous approach in an appropriate way.

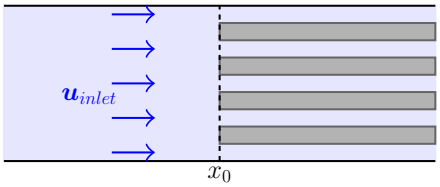

Figure 1: 2D fluid model.

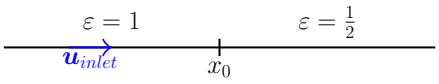

Figure 2: 1D porous model (ε the porosity).

The aim of this paper is to propose an alternative to the porous media approach, with two essential objectives: first, to circumvent the above mentioned difficulty, *i.e.* to allow to cope with discontinuous porosity media; second, to naturally boil down to the CFD model, when the mesh exactly fits the obstacles. To this purpose, we give up the derivation of an equivalent model at the continuous level. Instead, we directly integrate the balance equations over the control volumes, mimicking to some extent the usual finite-volume procedure, to the "real" fluid medium; doing so, integrals over the solid surfaces appear, for which expressions are given. In particular, a suitable treatment of the pressure forces naturally re-injects in the discrete system the above mentioned singular losses. Note that, conceptually, this procedure differs for a standard finite volume discretization of a set of PDEs: for instance, consistency and convergence issues make no more sense, since the discrete system cannot be seen associated to a continuous problem, up to the point at which the CFD model is recovered. In practice, we expect a significant gain in accuracy, at least for some solid obstacles geometry of interest; the numerical tests presented in this paper support this expectation. We also stress that, from an industrial point of view, gathering in the same numerical tool the capabilities of both the component and local approach is appealing, especially in a context of increasing computational power and thus, accordingly, a progressive drift toward more and more refined computations.

The proposed technique, which we refer to as the "integral approach", is applied here to compressible inviscid flows obeying the Euler equations, with general equation of states. We work here in the context of the open-source *Code_Saturne* software, using the same control volumes for both the scalar and velocity unknowns in a way consistent with a collocated finite volume scheme (see [13] for more details on finite volumes), and a fractional-step time discretization involving an elliptic step for a pressure correction (in other words, falling in the class of pressure correction algorithms [14, 15, 16, 17, 18, 19]), able to cope with all the Mach numbers regimes [20]. A first attempt to implement the integral approach with an explicit in time scheme (the so-called VFRoe-ncv approximate Godunov solver) may also be found in [21].

The paper outline is as follows. First, the multi-dimensional integral formulation of the compressible Euler equations is described. The time and spatial discretization of the formulation is proposed through a pressure-correction collocated finite volume scheme preserving the positivity of the density and the internal energy under a CFL condition based on the velocity of the fluid. Then, several fluid verification test cases are presented to illustrate the stability and the accuracy of this method with a numerical convergence analysis. The case of low Mach number flows is particularly investigated. Two one-

dimensional Riemann problems with an analytical thermodynamic law (Equation Of State (EOS)) are considered:

- a Riemann problem in a free domain using a stiffened gas EOS, modelling a gas or liquid fluid,
- a shock wave reflection on a wall using a stiffened gas EOS, the exact solution of which is detailed in Appendix C. This test corresponds to a water flow impacting an obstacle.

Finally, a two-dimensional **validation** test case with the integral approach in an obstructed medium is performed, where a pressure shock wave hits transversal rod bundles surrounded by a liquid; the formulation of the pressure forces on the solid boundaries takes here the same form as for the reflection boundary conditions used in the previous test, to deal within the integral approach framework with the macroscopic pressure jumps due to the sudden restriction of the flow passage section. Results are compared with a "reference" CFD computation, *i.e.* the 2D detailed solution, in particular through the evaluation of resultant forces acting on rods, to check that the integral approach indeed converges as expected towards the fine CFD computation when refining the mesh. From an industrial point of view, this latter test is reminiscent of a pressure wave impacting a rod bundle, as may occur in a reactor core during a Reactivity Initiated Accident [2].

2. An integral formulation

2.1. Set of governing equations

The compressible Euler equations (1) governing inviscid fluid flows are considered in an open subset of $\mathbb{R}^d$ ($d = 1, 2$ or 3) and in a bounded time interval $(0, T)$, $T \in \mathbb{R}_+^*$. The unknowns ρ, $\boldsymbol{u}$, P respectively denote the density, the velocity and the pressure of the fluid, while the momentum is $\boldsymbol{Q} = \rho\boldsymbol{u}$. The volumetric total energy E is such that:

$$E = \rho\left(\frac{\boldsymbol{u}^2}{2} + \epsilon(P,\rho)\right),$$

where the internal energy $\epsilon(P,\rho)$ is prescribed by the Equation Of State (EOS). Besides, in the right hand side of system (1), $\boldsymbol{f}$ is a mass external force and Φ_v a mass heat transfer source term. Thus the set of governing equations is:

$$\left\{\begin{array}{lcl} \partial_t\rho & + & \nabla\cdot\boldsymbol{Q} = 0, \\ \partial_t\boldsymbol{Q} & + & \boldsymbol{\nabla}\cdot(\boldsymbol{u}\otimes\boldsymbol{Q}) + \boldsymbol{\nabla}P = \rho\boldsymbol{f}, \\ \partial_t E & + & \nabla\cdot(\boldsymbol{u}(E+P)) = \rho\boldsymbol{f}\cdot\boldsymbol{u} + \rho\Phi_v. \end{array}\right. \tag{1}$$

The speed of sound, noted c, is such that:

$$c^2 = \left(\frac{P}{\rho^2} - \frac{\partial\epsilon(P,\rho)}{\partial\rho}\right) \Big/ \left(\frac{\partial\epsilon(P,\rho)}{\partial P}\right).$$

The EOS for a stiffened gas, which generalizes the usual ideal gas EOS and is used for a weakly compressible liquid (see [22]), is defined by

$$\rho\epsilon = \frac{P + \gamma\Pi_\infty}{\gamma - 1}, \tag{2}$$

with $\gamma > 1$ the heat capacity ratio and $\Pi_\infty \geq 0$ the stiffened gas pressure parameter. The admissible thermodynamic state is $P \in [-\Pi_\infty, +\infty)$. The speed of sound c is given by

$$c^2 = \frac{\gamma(P + \Pi_\infty)}{\rho}.$$

The specific enthalpy is $h = \epsilon(P, \rho) + \frac{P}{\rho}$, and the total enthalpy reads:

$$H = \frac{E + P}{\rho}.$$

Thereafter, $\boldsymbol{W}$ is the conservative variable:

$$\boldsymbol{W} = (\rho, \boldsymbol{Q}, E)^t.$$

The conservation laws (1) can be written as follows:

$$\partial_t \boldsymbol{W} + \boldsymbol{\nabla} \cdot \boldsymbol{F}(\boldsymbol{W}) = \boldsymbol{D}(\boldsymbol{W}), \tag{3}$$

where

$\boldsymbol{F}(\boldsymbol{W}) = (\boldsymbol{Q}, \boldsymbol{u} \otimes \boldsymbol{Q} + P\mathbf{I}, \boldsymbol{u}(E + P))^t$ is the convective flux,

$\boldsymbol{D}(\boldsymbol{W}) = (0, \rho \boldsymbol{f}, \rho(\boldsymbol{f} \cdot \boldsymbol{u} + \Phi_v))^t$ is the source term.

2.2. Integral form

The integral formulation of conservation laws described in [23] is considered. Set of equations (1) is integrated on control volumes Ω_i, $i \in \mathbb{N}$, which may contain many disjoint solid obstacles. All Ω_i cells form a mesh of the computational domain Ω, an open bounded connected polygonal subset of $\mathbb{R}^d$, such that $\overline{\Omega} = \cup_i \overline{\Omega}_i$ and $\cap_i \Omega_i = \emptyset$. Obstacles may be completely or partially included in Ω_i. Part of a control volume boundary may coincide with the surface of an obstacle. Figure 3 is a sketch of the admissible situations. The whole volume occupied by solid obstacles within the control volume Ω_i is denoted

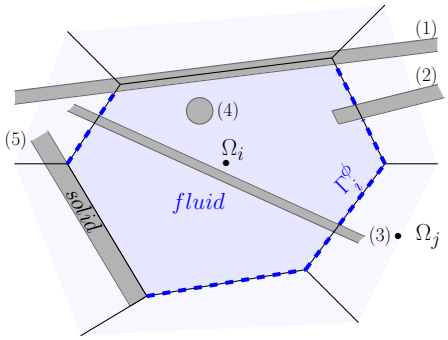

Figure 3: A (blue) control volume Ω_i includes (gray) obstacles numbered from 1 to 5. Obstacles may: overlap part of the boundary of Ω_i (1); partially occupy fluid cell (2); fully cross Ω_i and halve it (3); be totally included in Ω_i (4); or be aligned with part of the boundary of Ω_i (5). The dashed blue surface corresponds to the fluid part Γ_i^ϕ of the boundary of Ω_i.

by Ω_i^S. Thus, the volume occupied by fluid within Ω_i is $\Omega_i^\phi = \Omega_i \setminus \overline{\Omega_i^S}$. The mean value of the fluid state variable $\boldsymbol{W}(\mathbf{x}, t)$, with $\mathbf{x} \in \Omega$ and $t \in (0, T)$, over each fluid cell Ω_i^ϕ reads:

$$\boldsymbol{W}_i(t) = \frac{1}{\left|\Omega_i^\phi\right|} \int_{\Omega_i^\phi} \boldsymbol{W}(\mathbf{x}, t) \mathrm{d}\mathbf{x}.$$

Equation (3) is integrated over the bounded time interval $[t_0, t_1] \subset (0, T)$ and over the fluid cell Ω_i^ϕ. The flux-divergence theorem allows to get:

$$\left|\Omega_i^\phi\right|(\boldsymbol{W}_i(t_1) - \boldsymbol{W}_i(t_0)) + \int_{t_0}^{t_1}\int_{\Gamma_i} \boldsymbol{F}(\boldsymbol{W}(\mathbf{x},t)) \cdot \boldsymbol{n}(\mathbf{x}) \mathrm{d}\Gamma dt = \int_{t_0}^{t_1}\int_{\Omega_i^\phi} \boldsymbol{D}(\boldsymbol{W}(\mathbf{x},t)) \mathrm{d}\mathbf{x}\, dt, \quad (4)$$

where, $\Gamma_i = \partial\Omega_i^\phi$ denotes the whole boundary of the fluid cell Ω_i^ϕ with $\boldsymbol{n}(\mathbf{x})$ its unit outward normal vector. Fluid $\Gamma_i^\phi = \Gamma_i \setminus \partial\Omega_i^S$ and wall $\Gamma_i^w = \Gamma_i \cap \partial\Omega_i^S$ boundaries of each fluid cell Ω_i^ϕ are distinguished, such that:

$$\Gamma_i = \Gamma_i^\phi \cup \Gamma_i^w \quad \text{and} \quad \Gamma_i^\phi \cap \Gamma_i^w = \emptyset.$$

The integral formulation for all Ω_i holds:

$$\begin{aligned}\left|\Omega_i^\phi\right|(\boldsymbol{W}_i(t_1) - \boldsymbol{W}_i(t_0)) + \int_{t_0}^{t_1}\int_{\Gamma_i^\phi} \boldsymbol{F}(\boldsymbol{W}) \cdot \boldsymbol{n} \mathrm{d}\Gamma dt \; &+ \int_{t_0}^{t_1}\int_{\Gamma_i^w} \boldsymbol{F}(\boldsymbol{W}) \cdot \boldsymbol{n} \mathrm{d}\Gamma dt \\ &= \int_{t_0}^{t_1}\int_{\Omega_i^\phi} \boldsymbol{D}(\boldsymbol{W}) \mathrm{d}\mathbf{x}\, dt.\end{aligned} \quad (5)$$

The inner product between the normal $\boldsymbol{n}$ and the flux function $\boldsymbol{F}$ reads:

$$\boldsymbol{F}(\boldsymbol{W}) \cdot \boldsymbol{n} = (\rho \boldsymbol{u} \cdot \boldsymbol{n}, (\rho \boldsymbol{u} \cdot \boldsymbol{n})\, \boldsymbol{u} + P\boldsymbol{n}, (E + P)\, \boldsymbol{u} \cdot \boldsymbol{n})^t.$$

Note that the flux is null through Γ_i^w wall boundaries inside Ω_i, since $\boldsymbol{u} \cdot \boldsymbol{n}|_w = 0$, except the pressure flux $P\boldsymbol{n}|_w$.

In the sequel, the subscript ij refers to the interfaces between the neighbouring control volumes Ω_i and Ω_j, where $j \in V(i)$, and $V(i)$ defines the set of neighbouring cells of Ω_i. Besides, the superscript ϕ refers to the fluid volumes and the fluid interfaces ij where the fluid may cross the interface, noted Γ_{ij}^ϕ of measure $S_{ij}^\phi = \left|\Gamma_{ij}^\phi\right|$. The superscript w refers to solid interfaces where a wall boundary Γ_i^w of measure S_i^w is located inside the control volume Ω_i or on its boundary.

Remark 2.1. *In practice, the geometrical quantities, as defined in the integral formulation, have to be pre-processed. This step uses the mesh of the computational domain and the known geometry of the obstacles, for instance the multidimensional computer-aiding drafting (CAD). This pre-processing may turn to be tedious but it is performed once and can be parallelized in space.*

3. Time scheme

The time discretization of Equation (5) is based on an implicit first order Euler scheme. It is assumed that all numerical fluxes may be evaluated by means of a standard finite volume method, considering one mean value $\mathbf{W}_i^n$ per cell Ω_i at each time t^n, see [13] for more details. $\mathbf{W}_i^n$ is an approximation of $\boldsymbol{W}_i(t^n)$, and the time step at the n^{th} iteration is $\Delta t^n = t^{n+1} - t^n$. The numerical algorithm uses a pressure-correction scheme, with prediction and correction of the pressure [19, 20, 23].

Each time stepping is thus divided in three steps: first, the mass balance, which is used to update the density from ρ^n to ρ^{n+1}, and to predict a temporary pressure P^*

and a convective mass flux $\boldsymbol{Q}^* \cdot \boldsymbol{n}$, second, the momentum balance, where the velocity is updated from $\mathbf{u}^n$ to $\mathbf{u}^{n+1}$, and third, the last step, the energy balance that allows to update the total energy from E^n to E^{n+1} and thus to correct the pressure with the EOS. The superscript $(\cdot)^*$ states that the variable is predicted for the current step. The time semi-discrete algorithm is summarized below, starting with the initial condition $\mathbf{W}_i^n$ for all $n \in \mathbb{N}$:

1. Compute P^* solution of the mass balance, with $\delta\rho = \frac{\delta P}{(c^2)^n} = \frac{P^* - P^n}{(c^2)^n}$:

$$\frac{\delta P}{(c^2)^n} + \Delta t^n \nabla \cdot (\rho^n \mathbf{u}^n - \Delta t^n \boldsymbol{\nabla} P^*) = 0, \tag{6}$$

   and update:

$$\rho^{n+1} = \rho^n + \frac{\delta P}{(c^2)^n} \quad \text{and} \quad \boldsymbol{Q}^* = \rho^n \mathbf{u}^n - \Delta t^n \boldsymbol{\nabla} P^*. \tag{7}$$

2. Compute $\mathbf{u}^{n+1}$ solution of the momentum balance, with $\delta(\rho\mathbf{u}) = \rho^{n+1}\mathbf{u}^{n+1} - \rho^n\mathbf{u}^n$:

$$\delta(\rho\mathbf{u}) + \Delta t^n \boldsymbol{\nabla} \cdot \left(\mathbf{u}^{n+1} \otimes \boldsymbol{Q}^*\right) = -\Delta t^n \boldsymbol{\nabla} P^* + \Delta t^n \rho^{n+1} \boldsymbol{f}^n. \tag{8}$$

3. Compute E^{n+1} solution of the total energy balance, with $\delta E = E^{n+1} - E^n$:

$$\delta E + \Delta t^n \nabla \cdot \left(\frac{E^{n+1}}{\rho^{n+1}} \boldsymbol{Q}^*\right) = -\Delta t^n \nabla \cdot \left(\frac{P^*}{\rho^{n+1}} \boldsymbol{Q}^*\right) + \Delta t^n \rho^{n+1} \left(\boldsymbol{f}^n \cdot \mathbf{u}^{n+1} + \Phi_v^n\right), \tag{9}$$

   and update, using the EOS:

$$P^{n+1} = \mathcal{P}(\rho^{n+1}, \epsilon^{n+1}) \quad \text{with} \quad \epsilon^{n+1} = \frac{E^{n+1}}{\rho^{n+1}} - \frac{1}{2}(\mathbf{u}^{n+1} \cdot \mathbf{u}^{n+1}). \tag{10}$$

3.1. Mass balance

The pressure and the density are implicit, while the velocity and the entropy are considered frozen at time t^n. An acoustic mass flux $\boldsymbol{Q}^* \cdot \boldsymbol{n}$ is computed from the simplified momentum equation (14) given below. Integration of the mass balance equation, between t^n and t^{n+1} and over Ω_i^ϕ, gives the following implicit time scheme:

$$\left|\Omega_i^\phi\right| \left(\rho_i^{n+1} - \rho_i^n\right) + \Delta t^n \int_{\Gamma_i} \boldsymbol{Q}^* \cdot \boldsymbol{n} \mathrm{d}\Gamma = 0. \tag{11}$$

The acoustic linear approximation $(P_i^* - P_i^n) = (c^2)_i^n \left(\rho_i^{n+1} - \rho_i^n\right)$ is used, and reads $(c^2)_i^n = c^2(P_i^n, \rho_i^n)$. Equation (11) thus yields with the pressure variable:

$$\left|\Omega_i^\phi\right| \frac{1}{(c^2)_i^n} \left(P_i^* - P_i^n\right) + \Delta t^n \int_{\Gamma_i} \boldsymbol{Q}^* \cdot \boldsymbol{n} \mathrm{d}\Gamma = 0. \tag{12}$$

This step allows to predict the pressure P^*, from which the density ρ^{n+1} is deduced. For this purpose, the approximation of the implicit mass flux $\boldsymbol{Q}^* \cdot \boldsymbol{n}$ is, at interfaces:

$$\boldsymbol{Q}^* \cdot \boldsymbol{n} = \boldsymbol{Q}^n \cdot \boldsymbol{n} - \Delta t^n \boldsymbol{\nabla} P^* \cdot \boldsymbol{n}. \tag{13}$$

This discretization (13) is based on the simplified momentum balance:

$$\partial_t \boldsymbol{Q} + \boldsymbol{\nabla} P = 0. \tag{14}$$

Remark 3.1. *The relation* $\rho_i^{n+1} = \rho_i^n + \frac{1}{(c^2)_i^n}\left(P_i^* - P_i^n\right)$ *must be used for the update of the density to conserve the mass over time.*

Remark 3.2. *This first step can be viewed as an acoustic step: assuming a constant time step, Equations* (11) *and* (13)*, at the previous and current time level, yields the discrete wave equation below:*

$$\frac{\rho^{n+1} - 2\rho^n + \rho^{n-1}}{\Delta t^2} - \nabla \cdot \left(\left(c^2\right)^n \boldsymbol{\nabla}\rho^{n+1}\right) = 0.$$

Indeed, the semi-discrete acoustic linear system can be written:

$$\begin{cases} \dfrac{\rho^{n+1} - \rho^n}{\Delta t} + \nabla \cdot \boldsymbol{Q^*} = 0, \\ \dfrac{\boldsymbol{Q}^* - \boldsymbol{Q}^n}{\Delta t} + \boldsymbol{\nabla} P^*(\rho^{n+1}) = 0. \end{cases}$$

Combining the two equations yields:

$$\frac{\rho^{n+1} - \rho^n}{\Delta t} + \nabla \cdot \boldsymbol{Q^n} - \nabla \cdot (\Delta t \boldsymbol{\nabla} P^*(\rho^{n+1})) = 0.$$

Assuming that the mass flux $\boldsymbol{Q^n}$ *complies with the mass balance at the previous time step* t^n*:*

$$\frac{\rho^n - \rho^{n-1}}{\Delta t} + \nabla \cdot \boldsymbol{Q^n} = 0,$$

the wave equation, at the discrete level, can be thus obtained:

$$\frac{\rho^{n+1} - 2\rho^n + \rho^{n-1}}{\Delta t^2} - \nabla \cdot \boldsymbol{\nabla} P^*(\rho^{n+1}) = 0.$$

Using the acoustic linear approximation, $\boldsymbol{\nabla} P^*(\rho^{n+1}) = (c^2)^n \boldsymbol{\nabla}\rho^{n+1}$*, yields:*

$$\frac{\rho^{n+1} - 2\rho^n + \rho^{n-1}}{\Delta t^2} - \nabla \cdot \left(\left(c^2\right)^n \boldsymbol{\nabla}\rho^{n+1}\right) = 0.$$

3.2. Momentum balance

In this step, the velocity is implicit, whereas the density and the pressure are known from Equation (12) of the mass balance step, and the total energy is frozen. Integration of the momentum equation gives:

$$\left|\Omega_i^\phi\right| \left(\mathbf{Q}_i^{n+1} - \mathbf{Q}_i^n\right) + \Delta t^n \int_{\Gamma_i} (\boldsymbol{Q}^* \cdot \boldsymbol{n}) \mathbf{u}^{n+1} \mathrm{d}\Gamma + \Delta t^n \int_{\Gamma_i} P^* \boldsymbol{n} \mathrm{d}\Gamma - \Delta t^n \left|\Omega_i^\phi\right| \rho_i^{n+1} \boldsymbol{f}_i^n = 0. \tag{15}$$

This second step provides, for all Ω_i, the discrete unknown velocity $\mathbf{u}_i^{n+1}$. Thus the discrete momentum is inferred by $\mathbf{Q}_i^{n+1} = \rho_i^{n+1}\mathbf{u}_i^{n+1}$.

3.3. Energy balance

The total energy is implicit while the pressure, the density and the velocity are explicit from the previous steps. The total energy E_i^{n+1} is updated with the following implicit scheme:

$$\left|\Omega_i^\phi\right| \left(E_i^{n+1} - E_i^n\right) + \Delta t^n \int_{\Gamma_i} \frac{E^{n+1} + P^*}{\rho^{n+1}} (\boldsymbol{Q}^* \cdot \boldsymbol{n}) \mathrm{d}\Gamma \\ - \Delta t^n \left|\Omega_i^\phi\right| \left(\rho_i^{n+1} \boldsymbol{f}_i^n \cdot \mathbf{u}_i^{n+1} + \rho_i^{n+1} \Phi_{v,i}^n\right) = 0. \tag{16}$$

Finally, this third step provides the internal energy: $\epsilon_i^{n+1} = \dfrac{E_i^{n+1}}{\rho_i^{n+1}} - \dfrac{1}{2}\left(\mathbf{u}_i^{n+1} \cdot \mathbf{u}_i^{n+1}\right)$, and the pressure is thus corrected with the EOS: $\mathcal{P}(\rho, \epsilon)$, for all cells Ω_i:

$$P_i^{n+1} = \mathcal{P}(\rho_i^{n+1}, \epsilon_i^{n+1}).$$

4. Space scheme

A co-located finite volume method (all the variables are cell-based) is used to discretize in space the integral formulation of the conservation laws, Equation (5). At each step, a numerical flux is written to evaluate the different boundary integrals. We focus on the fluid and solid interior cell faces of the mesh defined in Section 2.2 (see Figure 3). The boundary conditions of the computational domain Ω are treated in Section 4.4. The space scheme is described for structured and orthogonal meshes, involving some simplifications particularly for the pressure gradient approximation in Equation (13).

4.1. Mass balance

In the time semi-discrete mass balance equation (12) given below, an expression of the mass flux needs to be specified:

$$\left|\Omega_i^\phi\right| \frac{1}{(c^2)_i^n} \left(P_i^* - P_i^n\right) + \Delta t^n \int_{\Gamma_i} \boldsymbol{Q}^* \cdot \boldsymbol{n} \mathrm{d}\Gamma = 0.$$

Note that the normal mass flux to the wall is null, $(\boldsymbol{Q} \cdot \boldsymbol{n})_{\Gamma^w} = \rho \boldsymbol{u} \cdot \boldsymbol{n}\big|_w = 0$, and thus:

$$\int_{\Gamma_i^w} \boldsymbol{Q}^* \cdot \boldsymbol{n} \mathrm{d}\Gamma = 0.$$

Equation (13), *i.e.* the simplified momentum balance, allows to decompose the integral over the fluid face into two integrals:

$$\int_{\Gamma_i} \boldsymbol{Q}^* \cdot \boldsymbol{n} \mathrm{d}\Gamma = \int_{\Gamma_i^\phi} \boldsymbol{Q}^* \cdot \boldsymbol{n} \mathrm{d}\Gamma = \underbrace{\int_{\Gamma_i^\phi} \boldsymbol{Q}^n \cdot \boldsymbol{n} \mathrm{d}\Gamma}_{1} - \underbrace{\int_{\Gamma_i^\phi} \Delta t^n \boldsymbol{\nabla} P^* \cdot \boldsymbol{n} \mathrm{d}\Gamma}_{2}. \tag{17}$$

4.1.1. Evaluation of the explicit mass flux

Integral 1 of Equation (17) is discretized for all cells Ω_i by summing up on all fluid interfaces Γ_{ij}^{ϕ} of Ω_i^{ϕ}, with $j \in V(i)$. The convective numerical flux is defined as follows:

$$\int_{\Gamma_i^{\phi}} \boldsymbol{Q}^n \cdot \boldsymbol{n} \mathrm{d}\Gamma = \sum_{j \in V(i)} \int_{\Gamma_{ij}^{\phi}} \boldsymbol{Q}^n \cdot \boldsymbol{n} \mathrm{d}\Gamma = \sum_{j \in V(i)} \left(\rho_{ij}^n\right)^{upw} \left(\mathbf{u}^n \cdot \boldsymbol{n}\right)_{ij} S_{ij}^{\phi}, \tag{18}$$

where $\boldsymbol{n}_{ij}$ is the unit normal vector at the fluid interface Γ_{ij}^{ϕ} from Ω_i^{ϕ} to Ω_j^{ϕ}. The transported quantity ρ_{ij}^n is estimated by the standard first order upwind scheme:

$$\left(\rho_{ij}^n\right)^{upw} = \beta_{ij}^n \rho_i^n + (1 - \beta_{ij}^n) \rho_j^n,$$

with:

$$\beta_{ij}^n = \begin{cases} 1 & \text{if } \left(\mathbf{u}^n \cdot \boldsymbol{n}\right)_{ij} \geq 0, \\ 0 & \text{otherwise.} \end{cases}$$

The normal velocity at the fluid interface is linearly interpolated between the two neighbouring cells:

$$\left(\mathbf{u}^n \cdot \boldsymbol{n}\right)_{ij} = \left(\alpha_{ij} \mathbf{u}_i^n + (1 - \alpha_{ij}) \mathbf{u}_j^n\right) \cdot \boldsymbol{n}_{ij},$$

where:

$$\alpha_{ij} = \frac{h_{ji}}{h_{ij} + h_{ji}},$$

and h_{ij} stands for the distance from the gravity centre of the cell Ω_i to the interface Γ_{ij}^{ϕ} (remember that we assumed an orthogonal structured grid).

4.1.2. Evaluation of the mass flux implicit contribution

As previously, integral 2 of Equation (17) is decomposed into a sum on all fluid faces of the cell Ω_i. Structured and orthogonal meshes are only considered, which allows a simple gradient scheme. Numerically and despite the potential presence of sub-elements into the cell, the value of the pressure P_i in the cell Ω_i is supposed uniform. The pressure gradient at the face is approximated with a "two-point flux approximation" scheme, standard for admissible meshes [24]:

$$\boldsymbol{\nabla} P \cdot \boldsymbol{n_{ij}} = \left.\frac{\partial P}{\partial \boldsymbol{n}}\right|_{\Gamma_{ij}^{\phi}} = \frac{P_j - P_i}{h_{ij} + h_{ji}}.$$

Thus, the scheme yields:

$$\int_{\Gamma_i^{\phi}} \Delta t^n \boldsymbol{\nabla} P^* \cdot \boldsymbol{n} \mathrm{d}\Gamma = \sum_{j \in V(i)} \int_{\Gamma_{ij}^{\phi}} \Delta t^n \boldsymbol{\nabla} P^* \cdot \boldsymbol{n} \mathrm{d}\Gamma = \sum_{j \in V(i)} \frac{\Delta t^n}{h_{ij} + h_{ji}} \left(P_j^* - P_i^*\right) S_{ij}^{\phi}. \tag{19}$$

We conclude that the mass flux is approximated, at each fluid interface, by:

$$\int_{\Gamma_i^{\phi}} \boldsymbol{Q}^* \cdot \boldsymbol{n} \mathrm{d}\Gamma = \sum_{j \in V(i)} \left(\rho_{ij}^n\right)^{upw} \left(\mathbf{u}^n \cdot \boldsymbol{n}\right)_{ij} S_{ij}^{\phi} - \sum_{j \in V(i)} \frac{\Delta t^n}{h_{ij} + h_{ji}} \left(P_j^* - P_i^*\right) S_{ij}^{\phi}. \tag{20}$$

4.2. Momentum balance

In this section, the semi-discrete momentum balance (15), solved with the velocity $\mathbf{u}^{n+1}$, is discretized in space:

$$\left|\Omega_i^\phi\right| \left(\rho_i^{n+1}\mathbf{u}_i^{n+1} - \rho_i^n \mathbf{u}_i^n\right) + \Delta t^n \int_{\Gamma_i} \mathbf{u}^{n+1}(\boldsymbol{Q}^* \cdot \boldsymbol{n})\mathrm{d}\Gamma + \Delta t^n \int_{\Gamma_i} P^* \boldsymbol{n}\mathrm{d}\Gamma - \Delta t^n \left|\Omega_i^\phi\right| \rho_i^{n+1} \boldsymbol{f}_i^n = 0.$$

At this step, the density ρ_i^{n+1} and the force $\boldsymbol{f}_i^n$ are known. We must define the numerical flux for both integrals of Equation (15):

$$\int_{\Gamma_i} \mathbf{u}^{n+1}(\boldsymbol{Q}^* \cdot \boldsymbol{n})\mathrm{d}\Gamma, \tag{21}$$

$$\text{and} \int_{\Gamma_i} P^* \boldsymbol{n}\mathrm{d}\Gamma. \tag{22}$$

4.2.1. Evaluation of the convective flux in the momentum equation

The integral (21) is decomposed on the wall faces Γ_i^w and the fluid faces Γ_i^ϕ of the cell Ω_i:

$$\int_{\Gamma_i} \mathbf{u}^{n+1}(\boldsymbol{Q}^* \cdot \boldsymbol{n})\mathrm{d}\Gamma = \underbrace{\int_{\Gamma_i^w} \mathbf{u}^{n+1}(\boldsymbol{Q}^* \cdot \boldsymbol{n})\mathrm{d}\Gamma}_{=0} + \int_{\Gamma_i^\phi} \mathbf{u}^{n+1}(\boldsymbol{Q}^* \cdot \boldsymbol{n})\mathrm{d}\Gamma.$$

To evaluate the fluid part in this relation, the numerical flux is summed up on all fluid interfaces Γ_{ij}^ϕ of the cell Ω_i as follows:

$$\int_{\Gamma_i^\phi} \mathbf{u}^{n+1}(\boldsymbol{Q}^* \cdot \boldsymbol{n})\mathrm{d}\Gamma = \sum_{j \in V(i)} \int_{\Gamma_{ij}^\phi} \mathbf{u}^{n+1}(\boldsymbol{Q}^* \cdot \boldsymbol{n})\mathrm{d}\Gamma = \sum_{j \in V(i)} \left(\mathbf{u}_{ij}^{n+1}\right)^{upw} (\boldsymbol{Q}^* \cdot \boldsymbol{n})_{ij} S_{ij}^\phi. \tag{23}$$

The mass flux $(\boldsymbol{Q}^* \cdot \boldsymbol{n})_{ij} S_{ij}^\phi$ has already been computed at the previous step by Equation (20):

$$(\boldsymbol{Q}^* \cdot \boldsymbol{n})_{ij} S_{ij}^\phi = \int_{\Gamma_{ij}^\phi} \boldsymbol{Q}^* \cdot \boldsymbol{n}\mathrm{d}\Gamma.$$

The value of the convected velocity $\left(\mathbf{u}_{ij}^{n+1}\right)^{upw}$ at the fluid interface is computed with a upwind scheme:

$$\left(\mathbf{u}_{ij}^{n+1}\right)^{upw} = \lambda_{ij}^n \mathbf{u}_i^{n+1} + (1 - \lambda_{ij}^n)\mathbf{u}_j^{n+1},$$

with:

$$\lambda_{ij}^n = \begin{cases} 1 & \text{if } (\boldsymbol{Q}^* \cdot \boldsymbol{n})_{ij} \geq 0, \\ 0 & \text{otherwise.} \end{cases}$$

4.2.2. Evaluation of the pressure force in the momentum equation

The pressure value P_i^* for all cells Ω_i is known from the mass conservation step. The integral decomposition on Γ_i^ϕ and Γ_i^w is thus explicit in time:

$$\int_{\Gamma_i} P^* \boldsymbol{n}\mathrm{d}\Gamma = \int_{\Gamma_i^w} P^* \boldsymbol{n}\mathrm{d}\Gamma + \int_{\Gamma_i^\phi} P^* \boldsymbol{n}\mathrm{d}\Gamma.$$

For the fluid interfaces Γ_{ij}^{ϕ}, the pressure contribution is a linear interpolation between neighbouring cells values, that is to say:

$$P_{ij}^{*} = \frac{h_{ij}P_{i}^{*} + h_{ji}P_{j}^{*}}{h_{ij} + h_{ji}} = (1 - \alpha_{ij})P_{i}^{*} + \alpha_{ij}P_{j}^{*}.$$

Remark 4.1. *Note that the interpolation coefficients $1-\alpha_{ij}$ are unusual. Indeed a standard interpolation formula would have yielded α_{ij} instead of $1-\alpha_{ij}$. This stems from the fact that the discrete pressure gradient is built as the transpose of the velocity divergence operator by duality with respect to the L^2 inner product [19].*

For the solid faces (interior walls) of Γ_{i}^{w}, two approximations of the wall pressure P^{w} are considered.

- *First approximation of the wall pressure*

The contribution of the wall pressure P^{w} is decentred in taking directly the cell centre value:

$$P^{w} = P_{i}^{*}. \tag{24}$$

Eventually, summing up on all cell faces, the pressure gradient may be written as follows:

$$\begin{aligned}\int_{\Gamma_i} P^{*}\boldsymbol{n}\mathrm{d}\Gamma = \left|\Omega_{i}^{\phi}\right| \boldsymbol{\nabla}_{i}P^{*} &= \sum_{j\in V(i)} P_{ij}^{*}\boldsymbol{n}_{ij}S_{ij}^{\phi} + \int_{\Gamma_i^w} P^{w}\boldsymbol{n}\mathrm{d}\Gamma \\ &= \sum_{j\in V(i)} P_{ij}^{*}\boldsymbol{n}_{ij}S_{ij}^{\phi} + P_{i}^{*}\left(-\sum_{j\in V(i)} \boldsymbol{n}_{ij}S_{ij}^{\phi}\right) \\ &= \sum_{j\in V(i)} \left(P_{ij}^{*} - P_{i}^{*}\right)\boldsymbol{n}_{ij}S_{ij}^{\phi}.\end{aligned}$$

In the last relation, we used the fact that the integral of the normal vector on a closed boundary vanishes:

$$\int_{\Gamma_i} \boldsymbol{n}\mathrm{d}\Gamma = 0 = \sum_{j\in V(i)} \boldsymbol{n}_{ij}S_{ij}^{\phi} + \int_{\Gamma_i^w} \boldsymbol{n}\mathrm{d}\Gamma.$$

- *Second approximation of the wall pressure*

Another choice for the evaluation of the wall pressure P^{w} is to use the "mirror state" technique defined in [25]. A virtual cell is considered in the solid obstacle with the normal $\boldsymbol{n}$ and the wall pressure is obtained by solving a Riemann problem, see Appendix B:

$$P^{w} = P^{Riemann}\left(\mathbf{W}_{i}^{n+1}, \widehat{\mathbf{W}}_{i}^{n+1}\right), \tag{25}$$

where

$$\widehat{\mathbf{W}}_{i}^{n+1} = \left[\rho_{i}^{n+1}, -\rho_{i}^{n+1}\mathbf{u}_{i}^{n+1}\cdot\boldsymbol{n}, E_{i}^{*}\right]^{t}$$

is the mirror state of

$$\mathbf{W}_{i}^{n+1} = \left[\rho_{i}^{n+1}, \rho_{i}^{n+1}\mathbf{u}_{i}^{n+1}\cdot\boldsymbol{n}, E_{i}^{*}\right]^{t}.$$

For the Euler equations (1) and for any EOS, the general form of the solution of this problem is:

$$P^{Riemann}\left(\mathbf{W}_i^{n+1}, \widehat{\mathbf{W}}_i^{n+1}\right) = P_i^* \left(1 + f\left(M^*\right)\right),$$

where M^* is the local Mach number based on the normal velocity to the wall:

$$M^* = \frac{\mathbf{u}_i^{n+1} \cdot \boldsymbol{n}}{c(P_i^*, \rho_i^{n+1})}.$$

The expression of the function f depends on the Riemann solver and the EOS of the fluid, see [25], but in any cases: $f(0) = 0$.

In order to compute the pressure integral contribution, the function f is linearized in using its Taylor expansion at the first order with respect to M^*, supposed to be small compared to 1:

$$P^w = P_i^* \left(1 + \hat{\gamma}\, M^*\right), \tag{26}$$

where $\hat{\gamma} = f'(0)$.

Remark 4.2. *For the EOS of an ideal gas, $\hat{\gamma} = \gamma$, and for the EOS of a stiffened gas, $\hat{\gamma} = \gamma\left(1 + \frac{\Pi_\infty}{P}\right)$.*

Consequently, the wall pressure integral evaluation becomes:

$$\begin{aligned}\int_{\Gamma_i^w} P^* \boldsymbol{n} \mathrm{d}\Gamma &= \int_{\Gamma_i^w} P_i^* \left(1 + \hat{\gamma}\, M^*\right) \boldsymbol{n} \mathrm{d}\Gamma \\ &= P_i^* \left(\int_{\Gamma_i^w} \boldsymbol{n} \mathrm{d}\Gamma\right) + P_i^* \frac{\hat{\gamma}}{c(P_i^*, \rho_i^{n+1})} \left(\int_{\Gamma_i^w} \boldsymbol{n}\boldsymbol{n}^t \mathrm{d}\Gamma\right) \mathbf{u}_i^{n+1}.\end{aligned}$$

The pressure gradient is thus discretized in space as:

$$\begin{aligned}\int_{\Gamma_i} P^* \boldsymbol{n} \mathrm{d}\Gamma = \left|\Omega_i^\phi\right| \boldsymbol{\nabla}_i P^* &= \sum_{j \in V(i)} P_{ij}^* \boldsymbol{n}_{ij} S_{ij}^\phi + \int_{\Gamma_i^w} P^w \boldsymbol{n} \mathrm{d}\Gamma \\ &= \sum_{j \in V(i)} \left(P_{ij}^* - P_i^*\right) \boldsymbol{n}_{ij} S_{ij}^\phi + \boldsymbol{K}_i \mathbf{u}_i^{n+1},\end{aligned}$$

where: $\boldsymbol{K}_i = \dfrac{\hat{\gamma} P_i^*}{c(P_i^*, \rho_i^{n+1})} \displaystyle\int_{\Gamma_i^w} \boldsymbol{n}\boldsymbol{n}^t \mathrm{d}\Gamma$ is a symmetric positive tensor.

Remark 4.3. *The first order term, $\boldsymbol{K}\mathbf{u}$, corresponds to a pressure drag force or form drag force due to the obstacle shape. This term dissipates kinetic energy and is not taken into account in the approximation (24).*

The resolution of the Riemann problem (25) seems more physically grounded than the first choice (24) of the cell pressure, particularly when the cell normal velocity to the wall is not close to zero. If the flow is locally tangent to the wall *i.e.* $M^* = 0$, then the second approximation boils down to the first one.

4.3. Energy balance

The space scheme is built from the semi-discrete equation (16) of the total energy conservation:

$$\left|\Omega_i^\phi\right|\left(E_i^{n+1}-E_i^n\right)+\Delta t^n\int_{\Gamma_i}\frac{E^{n+1}+P^*}{\rho^{n+1}}(\boldsymbol{Q}^*\cdot\boldsymbol{n})\mathrm{d}\Gamma \\ -\Delta t^n\left|\Omega_i^\phi\right|\left(\rho_i^{n+1}\boldsymbol{f}_i^n\cdot\mathbf{u}_i^{n+1}+\rho_i^{n+1}\Phi_{v,i}^n\right)=0.$$

The density ρ^{n+1}, the pressure P^* and the velocity $\mathbf{u}^{n+1}$ have been already computed in the previous steps, and the external force $\boldsymbol{f}^n$ and the term source Φ_v^n are given. Thus the last part of Equation (16) is explicit. The flux integral remains to be evaluated, once again by decomposing it on the fluid and solid faces:

$$\int_{\Gamma_i}\frac{E^{n+1}+P^*}{\rho^{n+1}}(\boldsymbol{Q}^*\cdot\boldsymbol{n})\mathrm{d}\Gamma=\underbrace{\int_{\Gamma_i^w}\frac{E^{n+1}+P^*}{\rho^{n+1}}(\boldsymbol{Q}^*\cdot\boldsymbol{n})\mathrm{d}\Gamma}_{=0}+\int_{\Gamma_i^\phi}\frac{E^{n+1}+P^*}{\rho^{n+1}}(\boldsymbol{Q}^*\cdot\boldsymbol{n})\mathrm{d}\Gamma. \tag{27}$$

The fluid part in the integral (27) is approximated for each cell Ω_i by a numerical flux. Using the definitions of Section 2.2, the flux is decomposed into a sum on all fluid interfaces of Γ_i^ϕ:

$$\int_{\Gamma_i^\phi}\frac{E^{n+1}+P^*}{\rho^{n+1}}(\boldsymbol{Q}^*\cdot\boldsymbol{n})\mathrm{d}\Gamma=\sum_{j\in V(i)}\int_{\Gamma_{ij}^\phi}\frac{E^{n+1}+P^*}{\rho^{n+1}}(\boldsymbol{Q}^*\cdot\boldsymbol{n})\mathrm{d}\Gamma \\ =\sum_{j\in V(i)}\left(\frac{E^{n+1}}{\rho^{n+1}}\right)_{ij}^{upw}(\boldsymbol{Q}^*\cdot\boldsymbol{n})_{ij}\,S_{ij}^\phi+\sum_{j\in V(i)}\left(\frac{P^*}{\rho^{n+1}}\right)_{ij}^{upw}(\boldsymbol{Q}^*\cdot\boldsymbol{n})_{ij}\,S_{ij}^\phi. \tag{28}$$

The fluid face values of $\left(\frac{E^{n+1}}{\rho^{n+1}}\right)_{ij}^{upw}$ and $\left(\frac{P^*}{\rho^{n+1}}\right)_{ij}^{upw}$ are given by an upwind scheme as described below:

$$\left(\frac{E^{n+1}}{\rho^{n+1}}\right)_{ij}^{upw}=\lambda_{ij}^n\frac{E_i^{n+1}}{\rho_i^{n+1}}+(1-\lambda_{ij}^n)\frac{E_j^{n+1}}{\rho_j^{n+1}},$$
$$\left(\frac{P^*}{\rho^{n+1}}\right)_{ij}^{upw}=\lambda_{ij}^n\frac{P_i^*}{\rho_i^{n+1}}+(1-\lambda_{ij}^n)\frac{P_j^*}{\rho_j^{n+1}},$$

where:

$$\lambda_{ij}^n=\begin{cases}1 & \text{if } (\boldsymbol{Q}^*\cdot\boldsymbol{n})_{ij}\geq 0,\\ 0 & \text{otherwise.}\end{cases}$$

4.4. Wall boundary conditions

Rigid wall boundary conditions on $\partial\Omega^w$, the wall boundary of the computational domain Ω, are taken into account by using the "mirror state" technique, see Appendix B and [26, 27, 25]. For the EOS of an ideal gas or stiffened gas, the exact solution of this Riemann problem is calculated. Hence the condition applied at a wall boundary face Γ_{b_i} of the boundary of Ω_i is such that the convective mass flux is null ($\boldsymbol{Q}_{b_i}^*\cdot\boldsymbol{n}_{b_i}=0$) and the predicted pressure is, for the EOS of an ideal gas, either:

- for $\mathbf{u}_i^n \cdot \boldsymbol{n}_{b_i} \leq 0$, rarefaction configuration:

$$\begin{cases} P_{b_i}^* = P_i^* \left(1 + \dfrac{\gamma-1}{2} \dfrac{\mathbf{u}_i^n \cdot \boldsymbol{n}_{b_i}}{c_i^n}\right)^{\frac{2\gamma}{\gamma-1}} & \text{if} \quad -\frac{2}{\gamma-1} < \frac{\mathbf{u}_i^n \cdot \boldsymbol{n}_{b_i}}{c_i^n} \leq 0, \\ P_{b_i}^* = 0 & \text{otherwise,} \end{cases}$$

- for $\mathbf{u}_i^n \cdot \boldsymbol{n}_{b_i} > 0$, shock configuration:

$$P_{b_i}^* = P_i^* \left(1 + \gamma \frac{\mathbf{u}_i^n \cdot \boldsymbol{n}_{b_i}}{c_i^n} \left(1 + \frac{(\gamma+1)^2}{16} \left(\frac{\mathbf{u}_i^n \cdot \boldsymbol{n}_{b_i}}{c_i^n}\right)^2\right)^{\frac{1}{2}} + \frac{\gamma(\gamma+1)}{4} \left(\frac{\mathbf{u}_i^n \cdot \boldsymbol{n}_{b_i}}{c_i^n}\right)^2\right).$$

Furthermore, the wall boundary value of the pressure for the EOS of a stiffened gas is inferred from the formula given in Appendix B.

5. Main properties of the scheme

5.1. Properties of the pressure prediction step

This section aims at proving that the numerical scheme preserves the positivity of both the discrete density and the predicted pressure.

The discrete equation coming from the time and space scheme of Equation (11) of the mass conservation is written with the notations introduced in Section 2.2 as follows:

$$\left|\Omega_i^\phi\right| \frac{(P_i^* - P_i^n)}{(c^2)_i^n} + \Delta t^n \sum_{j \in V(i)} \left(\beta_{ij}^n \rho_i^n + (1-\beta_{ij}^n)\rho_j^n\right) (\mathbf{u}^n \cdot \boldsymbol{n})_{ij} S_{ij}^\phi - \sum_{j \in V(i)} \frac{(\Delta t^n)^2}{h_{ij} + h_{ji}} \left(P_j^* - P_i^*\right) S_{ij}^\phi = 0. \tag{29}$$

Equation (29) yields a linear system:

$$\mathbf{A}\,\mathbf{X} = \mathbf{B},$$

with the vector $\mathbf{X} = (P_i^*)_{i \in \{1,\ldots,N_{cell}\}}$, where N_{cell} is the total number of cell (degrees of freedom). $\forall\, i \in \{1, ..., N_{cell}\}$, the diagonal matrix coefficients are:

$$A_{ii} = \begin{cases} \dfrac{\left|\Omega_i^\phi\right|}{(c^2)_i^n} + (\Delta t^n)^2 \displaystyle\sum_{j \in V(i)} \frac{S_{ij}^\phi}{h_{ij} + h_{ji}} & \text{if} \quad \left|\Omega_i^\phi\right| > 0, \\ 1 & \text{otherwise,} \end{cases}$$

$\forall\, i, j \in \{1, ..., N_{cell}\}$ with $j \neq i$, the off-diagonal coefficients are:

$$A_{ij} = \begin{cases} -\dfrac{(\Delta t^n)^2}{h_{ij} + h_{ji}} S_{ij}^\phi & \text{if} \quad j \in V(i) \text{ and } \left|\Omega_i^\phi\right| > 0, \\ 0 & \text{otherwise.} \end{cases}$$

The right hand side coefficients are:

$$B_i = \begin{cases} \left|\Omega_i^\phi\right| \dfrac{P_i^n}{(c^2)_i^n} - \Delta t^n \displaystyle\sum_{j \in V(i)} \left(\beta_{ij}^n \rho_i^n + (1-\beta_{ij}^n)\rho_j^n\right) (\mathbf{u}^n \cdot \boldsymbol{n})_{ij} S_{ij}^\phi & \text{if} \quad \left|\Omega_i^\phi\right| > 0, \\ P_i^n & \text{otherwise.} \end{cases}$$

Remark 5.1. *If the measure of the fluid part of the cell Ω_i is null, then all faces are considered as solid, i.e.: if $\left|\Omega_i^\phi\right| = 0$, then $\forall\, j \in V(i)$, $S_{ij}^\phi = 0$. We conclude that: $B_i = P_i^n$ and hence $P_i^* = P_i^n$.*

Property 5.1. *[Positivity of the density and the predicted pressure] Assume that the EOS is such that $\rho > 0$, $P > 0$ and $\hat{\gamma} = \frac{\rho c^2}{P} > 1$. If the initial conditions are such that, for all Ω_i, $\rho_i^n > 0$ and $P_i^n > 0$, then the density ρ_i^{n+1} and the pressure P_i^* will remain positive for all Ω_i, provided that the time step Δt^n complies with the CFL-like condition:*

$$\left|\Omega_i^\phi\right| \geq \hat{\gamma}\Delta t^n \sum_{j\in V(i)} \beta_{ij}^n \left(\mathbf{u}^n \cdot \boldsymbol{n}\right)_{ij} S_{ij}^\phi. \tag{30}$$

The CFL-like condition (30) allows to define the CFL^+ condition if $\left|\Omega_i^\phi\right| > 0$:

$$CFL^+ := \Delta t^n \max_{i\in\{1,\dots,N_{cell}\}} \frac{\hat{\gamma}}{\left|\Omega_i^\phi\right|} \sum_{j\in V(i)} \beta_{ij}^n \left(\mathbf{u}^n \cdot \boldsymbol{n}\right)_{ij} S_{ij}^\phi \leq 1. \tag{31}$$

Proof. The proof is that $\mathbf{A}$ is a M-matrix and $\mathbf{B}$ is positive.

- $\mathbf{A}$ is a M-matrix: the time step $\Delta t^n > 0$, $\forall\, i \in \{1, ..., N_{cell}\}$, $(c^2)_i^n > 0$ and $\left|\Omega_i^\phi\right| \geq 0$. Moreover, $\forall\, j \in V(i)$, $S_{ij}^\phi \geq 0$ and $h_{ij} + h_{ji} > 0$. Thus all diagonal coefficients of the matrix $\mathbf{A}$ are strictly positive ($A_{ii} > 0$), and all off-diagonal coefficients are negative or null ($A_{ij} \leq 0$ for $j \neq i$).

  $\forall\, i \in \{1, ..., N_{cell}\}$, $\mathbf{A}$ is strictly diagonally dominant by lines:

$$\begin{aligned} |A_{ii}| - \sum_{j\neq i} |A_{ij}| &= A_{ii} + \sum_{j\in V(i)} A_{ij} \\ &= \begin{cases} \frac{\left|\Omega_i^\phi\right|}{(c^2)_i^n} > 0 & \text{if } \left|\Omega_i^\phi\right| > 0, \\ 1 & \text{otherwise.} \end{cases} \end{aligned}$$

  Thus $\mathbf{A}$ is a M-matrix *i.e.* invertible and the $\mathbf{A}^{-1}$ coefficients are positive:

$$\forall\, i, j \in \{1, ..., N_{cell}\},\ \left(\mathbf{A}^{-1}\right)_{ij} \geq 0.$$

- $\mathbf{B}$ is positive: if $\left|\Omega_i^\phi\right| > 0$, the coefficient B_i yields:

$$B_i = \left[\frac{\left|\Omega_i^\phi\right|}{(c^2)_i^n} - \Delta t^n \sum_{j\in V(i)} \beta_{ij}^n \frac{\rho_i^n}{P_i^n} (\mathbf{u}^n \cdot \boldsymbol{n})_{ij} S_{ij}^\phi\right] P_i^n - \Delta t^n \sum_{j\in V(i)} (1 - \beta_{ij}^n) \rho_j^n (\mathbf{u}^n \cdot \boldsymbol{n})_{ij} S_{ij}^\phi. \tag{32}$$

  By considering Equation (32), the coefficient B_i is a positive combination of P_i^n and ρ_j^n if the CFL-like condition (30) holds. Thus the vector $\mathbf{B}$ is positive:

$$\forall\, i \in \{1, ..., N_{cell}\},\ B_i \geq 0.$$

Given that:

$$\mathbf{X} = \mathbf{A}^{-1}\mathbf{B},$$

we conclude, for all Ω_i, $X_i = P_i^* \geq 0$.

Likewise the density ρ^{n+1} remains positive under the condition (30). Indeed, to be conservative, we have set for all $i \in \{1, ..., N_{cell}\}$ (see Section 3) :

$$\rho_i^{n+1} - \rho_i^n = \frac{P_i^* - P_i^n}{(c^2)_i^n} \Rightarrow \rho_i^{n+1} = \frac{P_i^*}{(c_i^2)^n} + \rho_i^n \frac{(\hat{\gamma}_i^n - 1)}{\hat{\gamma}_i^n},$$

which completes the proof: $\rho_i^{n+1} > 0$, since $\hat{\gamma}_i^n = \hat{\gamma} > 1$.

Remark 5.2. *For an ideal gas, $\hat{\gamma} = \gamma \approx 1$ (notably $\gamma = 1.4$ for a diatomic gas). The CFL-like condition (30) is close to the standard CFL_u condition (33), based on the material transport.*

$$CFL_u := \Delta t^n \max_{i \in \{1,...,N_{cell}\}} \frac{1}{\left|\Omega_i^\phi\right|} \sum_{j \in V(i)} \beta_{ij}^n \left(\mathbf{u}^n \cdot \boldsymbol{n}\right)_{ij} S_{ij}^\phi \leq 1. \tag{33}$$

Remark 5.3. *For a liquid with a physical EOS, $\hat{\gamma} \gg 1$. This CFL-like condition (30) becomes more limiting than the standard CFL_u condition (33) on the velocity for an explicit upwind scheme. A way to maintain the standard CFL_u constraint is to substitute the mass balance linear scheme by a non-linear scheme (see Appendix A).*

Remark 5.4. *For the stiffened gas EOS, Property 5.1 does not apply. Indeed negative pressures greater than $-\Pi_\infty$ are meaningful. In this case, we may prove the following result, Property 5.2.*

Property 5.2. *[Admissible state of the density and the predicted pressure for the stiffened gas EOS] Assume a stiffened gas EOS (2), which is such that $\rho > 0$ and $P + \Pi_\infty > 0$. If the initial conditions are such that, for all Ω_i, $\rho_i^n > 0$ and $P_i^n + \Pi_\infty > 0$, then the density ρ_i^{n+1} and the pressure $P_i^* + \Pi_\infty$ will remain positive for all Ω_i, provided that the time step Δt^n complies with the modified CFL^+ condition:*

$$CFL^+ := \gamma \Delta t^n \max_{i \in \{1,...,N_{cell}\}} \frac{1}{\left|\Omega_i^\phi\right|} \sum_{j \in V(i)} \beta_{ij}^n \left(\mathbf{u}^n \cdot \boldsymbol{n}\right)_{ij} S_{ij}^\phi \leq 1. \tag{34}$$

Proof. The proof is identical to the one of Property 5.1 thanks to the suitable change of variables, for all Ω_i, $\widetilde{P}_i = P_i + \Pi_\infty$ in the discrete mass balance equation (29).

Remark 5.5. *The CFL^+ condition (34) remains always close to the CFL_u condition (33), since, for the stiffened gas EOS, γ is usually in the range $(1, 10]$.*

Remark 5.6 (Conservativity in time and space). *The algorithm is conservative in time and in space. It is important to emphasize that, for all $i \in \{1, ..., N_{cell}\}$, the density ρ_i^{n+1} needs to be updated only as follows:*

$$\rho_i^{n+1} = \rho_i^n + \frac{1}{(c_i^2)^n} \left(P_i^* - P_i^n\right).$$

Conservativity of the algorithm allows to find the correct shock solutions in pure fluid cases. This is verified in presence of discontinuities in [20]. The convergence order, determined from the Riemann problem of the shock tube test case, is $\frac{1}{2}$ for contact discontinuities, and 1 for shock waves and rarefaction waves.

5.2. Properties of the pressure correction step

This section aims at proving that the numerical scheme preserves the positivity of the discrete internal energy and hence of the corrected pressure.

Property 5.3. *[Positivity of the internal energy] Assume that the EOS is such that $\rho > 0$ and $\epsilon > 0$. If the initial conditions are such that, for all Ω_i, $\rho_i^n > 0$ and $\epsilon_i^n > 0$, then the internal energy ϵ_i^{n+1} will remain positive for all Ω_i, provided that the time step Δt^n complies with the CFL-like condition:*

$$\left|\Omega_i^\phi\right| \geq \frac{\Delta t^n}{\rho_i^n \epsilon_i^n} \sum_{j \in V(i)} \left(\left(\frac{P^*}{\rho^{n+1}} \right)_{ij}^{upw} (\boldsymbol{Q}^* \cdot \boldsymbol{n})_{ij} - \left(P_{ij}^* - P_i^*\right) \boldsymbol{n}_{ij} \cdot \mathbf{u}_i^{n+1} \right) S_{ij}^\phi. \tag{35}$$

The CFL-like condition (35) allows to define the CFL_ϵ^+ condition, if $\left|\Omega_i^\phi\right| > 0$:

$$CFL_\epsilon^+ := \Delta t^n \max_{i \in \{1,\dots,N_{cell}\}} \frac{1}{\left|\Omega_i^\phi\right|} \frac{a_i^*}{\rho_i^n \epsilon_i^n} \leq 1, \tag{36}$$

with $a_i^* := \sum_{j \in V(i)} \left(\left(\frac{P^*}{\rho^{n+1}} \right)_{ij}^{upw} (\boldsymbol{Q}^* \cdot \boldsymbol{n})_{ij} - \left(P_{ij}^* - P_i^*\right) \boldsymbol{n}_{ij} \cdot \mathbf{u}_i^{n+1} \right) S_{ij}^\phi.$

Proof. The proof consists in deriving a discrete kinetic energy balance. Subtracting this balance to the total energy balance (16) allows to obtain a discrete internal energy balance and to deduce a condition of positivity on the right hand side of the associated linear system.

- Discrete kinetic energy balance

The derivation of the kinetic energy balance in the continuous case is mimicked: we multiply the momentum equation by the velocity and use the mass balance. Multiplying the discrete momentum balance (15) by the velocity $\mathbf{u}_i^{n+1}$ for all Ω_i, $i \in \{1, ..., N_{cell}\}$, yields:

$$\begin{aligned} \left|\Omega_i^\phi\right| \frac{\rho_i^{n+1}\mathbf{u}_i^{n+1} - \rho_i^n \mathbf{u}_i^n}{\Delta t^n} \cdot \mathbf{u}_i^{n+1} + \sum_{j \in V(i)} (\boldsymbol{Q}^* \cdot \boldsymbol{n})_{ij} \left(\mathbf{u}_{ij}^{n+1}\right)^{upw} \cdot \mathbf{u}_i^{n+1} S_{ij}^\phi \\ + \sum_{j \in V(i)} \left(P_{ij}^* - P_i^*\right) \boldsymbol{n}_{ij} \cdot \mathbf{u}_i^{n+1} S_{ij}^\phi = 0. \end{aligned} \tag{37}$$

Using the identity: $2\ \mathbf{u}_i^n \cdot \mathbf{u}_i^{n+1} = \left|\mathbf{u}_i^{n+1}\right|^2 + \left|\mathbf{u}_i^n\right|^2 - \left|\mathbf{u}_i^{n+1} - \mathbf{u}_i^n\right|^2$, the unsteady term of Equation (37) reads:

$$2\left(\rho_i^{n+1}\left|\mathbf{u}_i^{n+1}\right|^2 - \rho_i^n \mathbf{u}_i^n \cdot \mathbf{u}_i^{n+1}\right) = 2\rho_i^{n+1}\left|\mathbf{u}_i^{n+1}\right|^2 - \rho_i^n\left|\mathbf{u}_i^n\right|^2 + \rho_i^n\left|\mathbf{u}_i^{n+1} - \mathbf{u}_i^n\right|^2 - \rho_i^n\left|\mathbf{u}_i^{n+1}\right|^2,$$

multiplying the mass balance (11) by $\frac{1}{2}\left|\mathbf{u}_i^{n+1}\right|^2$,

$$\frac{\left|\Omega_i^\phi\right|}{2\Delta t^n}\rho_i^n\left|\mathbf{u}_i^{n+1}\right|^2 = \frac{\left|\Omega_i^\phi\right|}{2\Delta t^n}\rho_i^{n+1}\left|\mathbf{u}_i^{n+1}\right|^2 + \sum_{j \in V(i)} (\boldsymbol{Q}^* \cdot \boldsymbol{n})_{ij} \frac{1}{2}\left|\mathbf{u}_i^{n+1}\right|^2 S_{ij}^\phi,$$

and substituting this relation in Equation (37) yields:

$$\frac{\left|\Omega_i^\phi\right|}{2\Delta t^n}\left(\rho_i^{n+1}\left|\mathbf{u}_i^{n+1}\right|^2-\rho_i^n\left|\mathbf{u}_i^n\right|^2\right)+\sum_{j\in V(i)}\left(\boldsymbol{Q}^*\cdot\boldsymbol{n}\right)_{ij}\left(\left(\mathbf{u}_{ij}^{n+1}\right)^{upw}\cdot\mathbf{u}_i^{n+1}-\frac{1}{2}\left|\mathbf{u}_i^{n+1}\right|^2\right)S_{ij}^\phi$$
$$+\frac{\left|\Omega_i^\phi\right|}{2\Delta t^n}\rho_i^n\left|\mathbf{u}_i^{n+1}-\mathbf{u}_i^n\right|^2+\sum_{j\in V(i)}\left(P_{ij}^*-P_i^*\right)\boldsymbol{n}_{ij}\cdot\mathbf{u}_i^{n+1}S_{ij}^\phi=0. \tag{38}$$

The convective flux can be rewritten for the upwind discretization (23) as:

$$\left(\boldsymbol{Q}^*\cdot\boldsymbol{n}\right)_{ij}\left(\left(\mathbf{u}_{ij}^{n+1}\right)^{upw}\cdot\mathbf{u}_i^{n+1}-\frac{1}{2}\left|\mathbf{u}_i^{n+1}\right|^2\right)=\left(\boldsymbol{Q}^*\cdot\boldsymbol{n}\right)_{ij}\frac{1}{2}\left|\left(\mathbf{u}_{ij}^{n+1}\right)^{upw}\right|^2$$
$$-\underbrace{\left(1-\lambda_{ij}^n\right)\left(\boldsymbol{Q}^*\cdot\boldsymbol{n}\right)_{ij}}_{\leq 0}\frac{1}{2}\left|\mathbf{u}_i^{n+1}-\mathbf{u}_j^{n+1}\right|^2.$$

The coefficient λ_{ij}^n has been defined in Section 4.2.1. Eventually substituting this latter equality in Equation (38) yields the following discrete kinetic energy balance for all Ω_i:

$$\frac{\left|\Omega_i^\phi\right|}{2\Delta t^n}\left(\rho_i^{n+1}\left|\mathbf{u}_i^{n+1}\right|^2-\rho_i^n\left|\mathbf{u}_i^n\right|^2\right)+\sum_{j\in V(i)}\left(\boldsymbol{Q}^*\cdot\boldsymbol{n}\right)_{ij}\frac{1}{2}\left|\left(\mathbf{u}_{ij}^{n+1}\right)^{upw}\right|^2S_{ij}^\phi$$
$$+\sum_{j\in V(i)}\left(P_{ij}^*-P_i^*\right)\boldsymbol{n}_{ij}\cdot\mathbf{u}_i^{n+1}S_{ij}^\phi+R_i^2=0, \tag{39}$$

with $R_i^2=\dfrac{\left|\Omega_i^\phi\right|}{2\Delta t^n}\rho_i^n\left|\mathbf{u}_i^{n+1}-\mathbf{u}_i^n\right|^2-\displaystyle\sum_{j\in V(i)}\left(1-\lambda_{ij}^n\right)\left(\boldsymbol{Q}^*\cdot\boldsymbol{n}\right)_{ij}\frac{1}{2}\left|\mathbf{u}_i^{n+1}-\mathbf{u}_j^{n+1}\right|^2S_{ij}^\phi\geq 0$, since $\rho_i^n>0$ for all Ω_i.

- Discrete internal energy balance

Subtracting the discrete kinetic energy balance (39) to the discrete total energy balance (16) yields the following local discrete internal energy balance for all Ω_i:

$$\frac{\left|\Omega_i^\phi\right|}{\Delta t^n}\left(\rho_i^{n+1}\epsilon_i^{n+1}-\rho_i^n\epsilon_i^n\right)+\sum_{j\in V(i)}\left(\boldsymbol{Q}^*\cdot\boldsymbol{n}\right)_{ij}\left(\epsilon_{ij}^{n+1}\right)^{upw}S_{ij}^\phi$$
$$+\sum_{j\in V(i)}\left(\left(\boldsymbol{Q}^*\cdot\boldsymbol{n}\right)_{ij}\left(\frac{P^*}{\rho^{n+1}}\right)_{ij}^{upw}-\left(P_{ij}^*-P_i^*\right)\boldsymbol{n}_{ij}\cdot\mathbf{u}_i^{n+1}\right)S_{ij}^\phi=R_i^2. \tag{40}$$

The upwind discretization of the internal energy equation (40) infers that the associated linear system matrix is a M-matrix, *i.e.* invertible and its inverse is positive. Thus the internal energy ϵ_i^{n+1} remains positive as long as the explicit-in-time term is positive. Since $R_i^2\geq 0$, the sufficient condition of the positivity of ϵ_i^{n+1} is for all Ω_i:

$$\frac{\left|\Omega_i^\phi\right|}{\Delta t^n}\rho_i^n\epsilon_i^n+\sum_{j\in V(i)}\left(\left(P_{ij}^*-P_i^*\right)\boldsymbol{n}_{ij}\cdot\mathbf{u}_i^{n+1}-\left(\frac{P^*}{\rho^{n+1}}\right)_{ij}^{upw}\left(\boldsymbol{Q}^*\cdot\boldsymbol{n}\right)_{ij}\right)S_{ij}^\phi\geq 0,$$

which completes the proof.

Remark 5.7. *The positivity of the pressure holds under the CFL-like conditions (30) and (35): for all Ω_i, $P_i^{n+1} = \mathcal{P}(\rho_i^{n+1}, \epsilon_i^{n+1}) \geq 0$, since $\rho_i^{n+1} > 0$ under the CFL^+ condition (30) and $\epsilon_i^{n+1} \geq 0$ under the CFL_ϵ^+ condition (35).*

Remark 5.8. *if $\left|\Omega_i^\phi\right| = 0$, then $\forall\, j \in V(i)$, $S_{ij}^\phi = 0$. We thus conclude that $\rho_i^{n+1} = \rho_i^n$ and $\epsilon_i^{n+1} = \epsilon_i^n$ (and so $P_i^{n+1} = P_i^n$) for all Ω_i.*

Remark 5.9. *For the stiffened gas EOS, Property 5.3 does not apply. The inequality $\rho\epsilon - \Pi_\infty \geq 0$, equivalent to $P + \Pi_\infty \geq 0$ with $\gamma > 1$, must be verified. The change of variables is set here $\widetilde{\rho\epsilon} = \rho\epsilon - \Pi_\infty$ and $\widetilde{P} = P + \Pi_\infty$, given that $\widetilde{P} = (\gamma - 1)\widetilde{\rho\epsilon}$. In this case, we may prove the following result, Property 5.4.*

Property 5.4. *[Admissible state of the internal energy for the stiffened gas EOS] Assume a stiffened gas EOS (2), which is such that $\rho > 0$ and $\widetilde{\rho\epsilon} = \rho\epsilon - \Pi_\infty > 0$. If the initial conditions are such that for all Ω_i, $\rho_i^n > 0$ and $\widetilde{\rho\epsilon}_i^n > 0$, then $\widetilde{\rho\epsilon}_i^{n+1}$ will remain positive for all Ω_i, provided that the time step Δt^n complies with the modified CFL_ϵ^+ condition:*

$$CFL_\epsilon^+ := (\gamma - 1)\Delta t^n \max_{i \in \{1,\dots,N_{cell}\}} \frac{1}{\left|\Omega_i^\phi\right|} \frac{\tilde{a}_i^*}{\widetilde{P}_i^n} \leq 1, \tag{41}$$

$$\text{with } \tilde{a}_i^* := \sum_{j \in V(i)} \left(\left(\frac{\widetilde{P}^*}{\rho^{n+1}} \right)_{ij}^{upw} (\boldsymbol{Q}^* \cdot \boldsymbol{n})_{ij} - \left(\widetilde{P}_{ij}^* - \widetilde{P}_i^* \right) \boldsymbol{n}_{ij} \cdot \mathbf{u}_i^{n+1} \right) S_{ij}^\phi.$$

Proof. The proof is identical to the one of Property 5.3 thanks to the suitable change of variables (see Remark 5.9), for all Ω_i, $\widetilde{P}_i = P_i + \Pi_\infty$ and $\widetilde{\rho\epsilon}_i = \rho_i\epsilon_i - \Pi_\infty$ in the proof of Property 5.3 and thus in the discrete internal energy balance equation (40).

Remark 5.10. *Note that, when considering a locally constant pressure, the CFL_ϵ^+ condition (41) boils down to:*

$$(\gamma - 1)\Delta t^n \max_{i \in \{1,\dots,N_{cell}\}} \frac{1}{\left|\Omega_i^\phi\right|} \sum_{j \in V(i)} \frac{(\boldsymbol{Q}^* \cdot \boldsymbol{n})_{ij}}{\left(\rho_{ij}^{n+1}\right)^{upw}} S_{ij}^\phi \leq 1,$$

the CFL_ϵ^+ number (41) is thus approximately equal to $(\gamma - 1)CFL_u$, and $(\gamma - 1)$ is of the same order of magnitude as one.

6. Numerical results

6.1. Verification test cases: one-dimensional Riemann problems

6.1.1. Sod shock tube

This section is dedicated to the verification case of the basic configuration without obstacles: the so-called Sod shock tube, which is an one-dimensional Riemann problem. The computational domain is $\Omega = (-200, 200)$ and consists of a one-dimensional tube with a membrane in the middle which separates two different constant fluid states. At the time $t = 0$, the membrane bursts. The ideal gas EOS is considered with $\gamma = 1.4$ (diatomic gas). The numerical solution is compared with the exact solution, which is composed of a 1-rarefaction wave followed by a 2-contact discontinuity and a 3-shock wave. This solution is derived in [28].

All meshes used to solve this Riemann problem are uniform. The meshes contain N cells with $N = 800, 1600, 3200, 6400, 12800, 25600$ or 51200. The CFL_u number, based on the material velocity u and defined by Equation (33), is equal to 0.1. In the sequel, the space step dx is defined in m, the density ρ in $kg.m^{-3}$, the velocity u in $m.s^{-1}$ and the pressure P in Pa.

Initial conditions are, for the left and right states:

$$\begin{cases} (\rho_L, u_L, P_L) = (1, 0, 10^5)\,, \\ (\rho_R, u_R, P_R) = (0.125, 0, 10^4)\,. \end{cases} \tag{42}$$

For a qualitative study, the profiles of density, velocity, pressure and enthalpy are presented in Figure 4 at a time $t = 0.3\ s$ such that all waves are visible in the computational domain. The exact profiles are recovered with numerical diffusion for the rarefaction, contact discontinuity and shock waves. To check the convergence order, we plot in Figure 5 the logarithm of the relative L^1 error[1] as a function of the logarithm of the mesh size N (see Table 1). The numerical rates of convergence are about 0.6 for the density, 0.9 for the velocity and the pressure, and slightly more than 0.5 for the enthalpy (see Table 2). Theoretically the convergence order is 1 for a rarefaction wave and shock wave, and $\frac{1}{2}$ for a contact discontinuity. This verification shows the ability of the fractional step scheme to correctly capture discontinuous solutions.

dx	N	ρ	u	P	h
5.0e-1	800	8.497e-3	9.778e-3	5.308e-3	9.099e-3
2.5e-1	1600	5.427e-3	5.627e-3	3.010e-3	6.180e-3
1.25e-1	3200	3.472e-3	3.078e-3	1.679e-3	4.169e-3
6.25e-2	6400	2.237e-3	1.668e-3	9.272e-4	2.831e-3
3.125e-2	12800	1.456e-3	9.269e-3	5.095e-4	1.943e-3
1.5625e-2	25600	9.571e-4	5.070e-4	2.780e-4	1.342e-3
7.8125e-3	51200	6.354e-4	2.660e-4	1.496e-4	9.273e-4

Table 1: L^1 error for variables (ρ, u, P, h) for all the considered meshes for the Sod shock-tube.

[1]The discrete relative L^1 error is defined as: $e_{L^1(\Omega)}(\psi) = \frac{\sum_{i=1}^{N_{cell}} \left|\psi_i^{exact} - \psi_i^{compute}\right| meas(\Omega_i)}{\sum_{i=1}^{N_{cell}} \left|\psi_i^{exact}\right| meas(\Omega_i)}$.

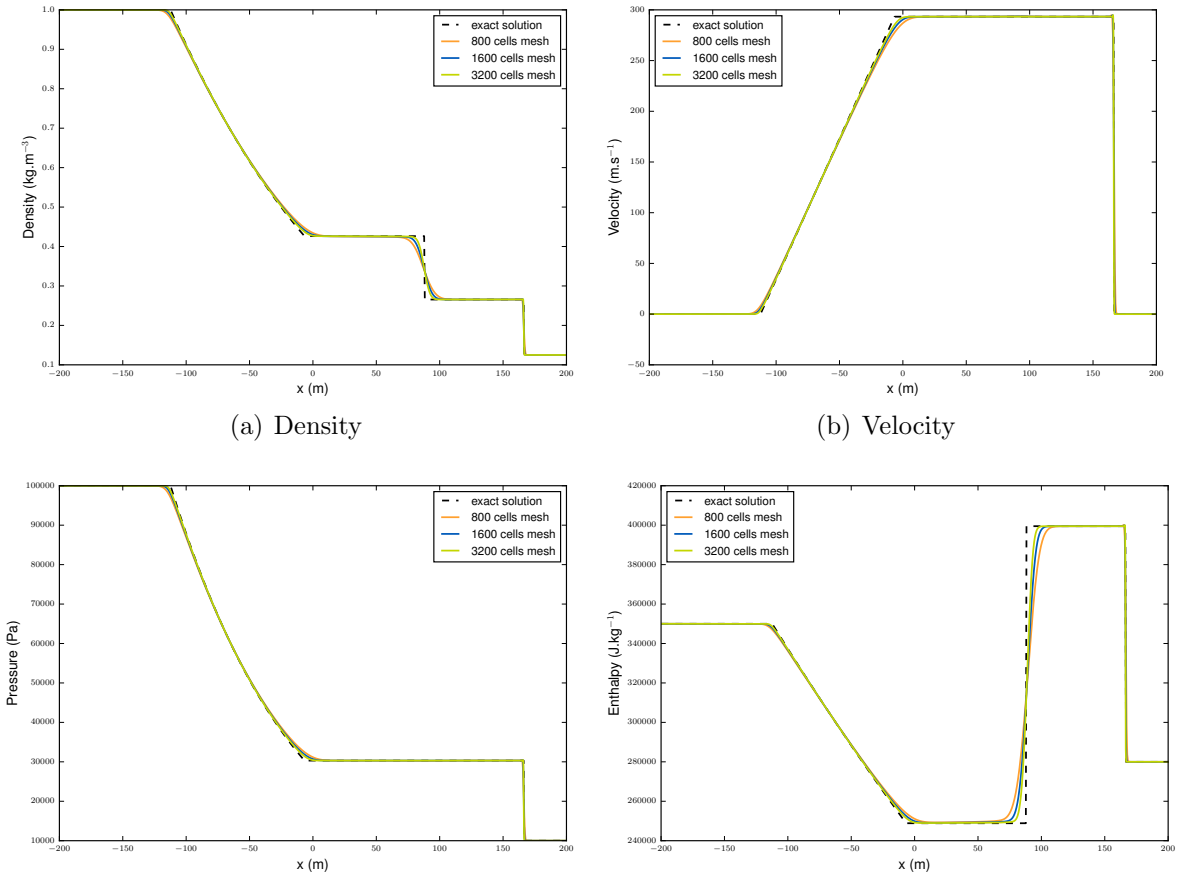

(a) Density (b) Velocity

(c) Pressure (d) Enthalpy

Figure 4: Comparison of the numerical solutions for 800, 1600 and 3200 cells with the exact solution for the Sod shock-tube at $t = 0.3\ s$.

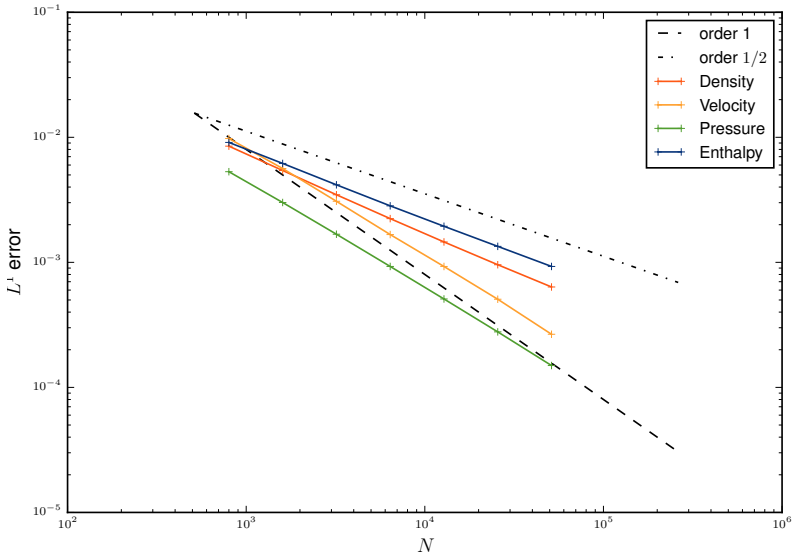

Figure 5: L^1 convergence curves for the Sod shock-tube.

dx	N	ρ cnv. order	u cnv. order	P cnv. order	h cnv. order
5.0e-1	800				
2.5e-1	1600	0.6467	0.7972	0.8185	0.5582
1.25e-1	3200	0.6444	0.8703	0.8436	0.5679
6.25e-2	6400	0.6341	0.8839	0.8562	0.5586
3.125e-2	12800	0.6196	0.8477	0.8638	0.5429
1.5625e-2	25600	0.6054	0.8703	0.8743	0.5337
7.8125e-3	51200	0.5910	0.9306	0.8940	0.5334

Table 2: L^1 convergence order for variables (ρ, u, P, h) for all the considered meshes for the Sod shock-tube.

6.1.2. Riemann problem with a stiffened gas EOS

This verification test case is a one-dimensional Riemann problem with a stiffened gas EOS. The stiffened gas parameters are computed for a liquid water at a 165 *bar* pressure and 583.15 K temperature: $\gamma_{SG} = 1.85768$ and $\Pi_\infty = 4.243468 \times 10^8$ Pa. Initial conditions are, for the left and right states:

$$\begin{cases} (\rho_L, u_L, P_L) = (800, 0, 1.65 \times 10^7)\,, \\ (\rho_R, u_R, P_R) = (797, 6.827, 5.0 \times 10^6)\,. \end{cases} \tag{43}$$

This test case corresponds to a low Mach number flow. The Mach number is such that: $M = \frac{|u|}{c} \in [0, 10^{-2}]$. The exact solution is composed of a 1-rarefaction wave followed by a 2-contact discontinuity and a 3-shock wave. The uniform meshes contain $N = 800$, 1600, 3200, 6400, 12800, 25600 and 51200 cells. For the first test, CFL_u is equal to 0.0084, *i.e.* $CFL^+ = 0.015$ (CFL^+ defined by Equation (31)). The second test is run with CFL_u equal to 0.54 ($CFL^+ = 1$). The simulation ending time is 0.1 s. As expected, the numerical simulation matches the exact profile with numerical diffusion at discontinuities (see Figure 6 and Table 3). The greater is the CFL_u value, the greater is the diffusion, excepted for the contact discontinuity profile which maintains sharp (see Figure 8 and Table 5). In accordance with the theory for a stiffened gas EOS, we note that the L^1 convergence order is $\frac{1}{2}$ for all waves (see Table 4, 6 and Figure 7, 9).

The semi-implicit pressure correction scheme allows to release the explicit stability constraint due to the acoustic waves and thus to increase the CFL_u value.

Test case 1 with $CFL^+ = 0.015$

dx	N	ρ	u	P	h
5.0e-01	800	1.927e-04	2.546e-02	1.534e-02	1.684e-04
2.5e-01	1600	1.352e-04	1.786e-02	1.073e-02	1.182e-04
1.25e-01	3200	9.449e-05	1.244e-02	7.477e-03	8.260e-05
6.25e-02	6400	6.570e-05	8.634e-03	5.189e-03	5.744e-05
3.125e-02	12800	4.534e-05	5.943e-03	3.571e-03	3.965e-05
1.5625e-02	25600	3.100e-05	4.049e-03	2.433e-03	2.712e-05
7.8125e-03	51200	2.093e-05	2.722e-03	1.635e-03	1.832e-05

Table 3: L^1 error for variables (ρ, u, P, h) for all the considered meshes for a Riemann problem with a SG EOS ($CFL^+ = 0.015$).

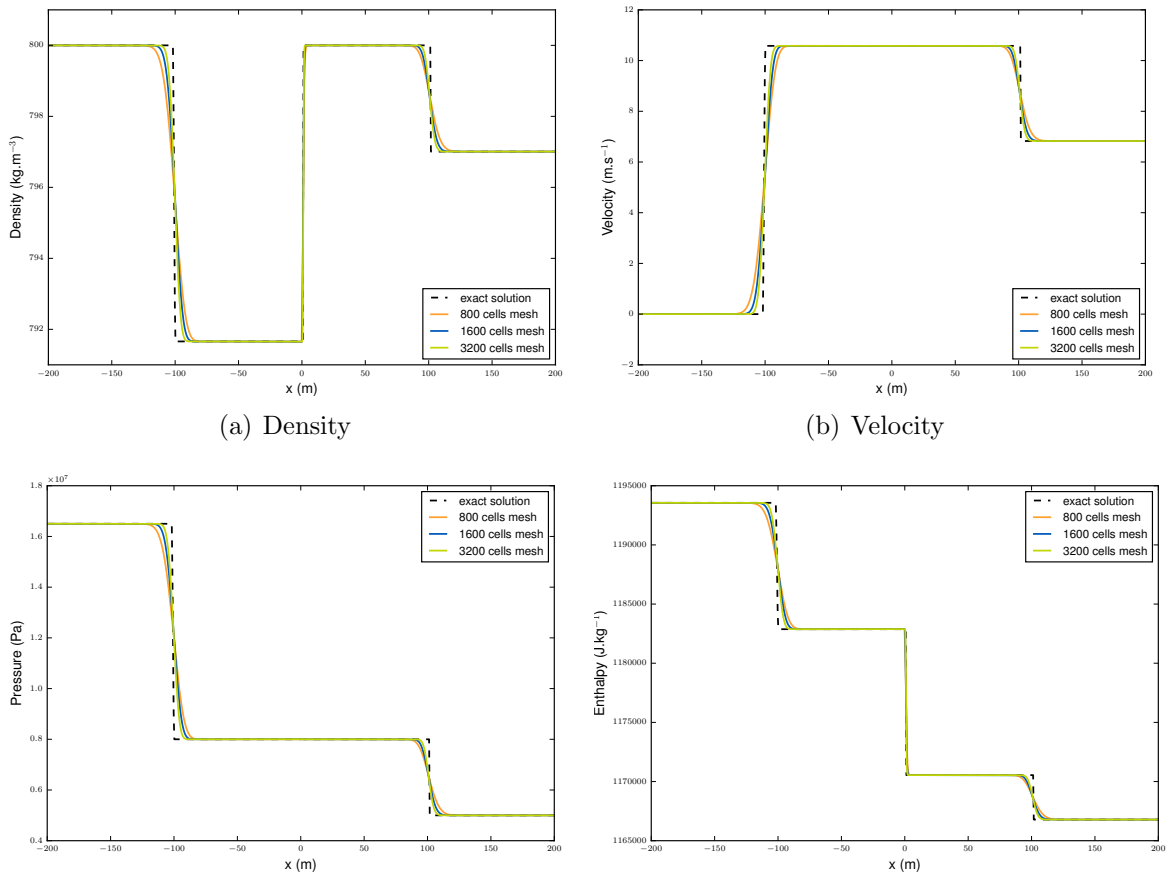

(a) Density (b) Velocity

(c) Pressure (d) Enthalpy

Figure 6: Comparison of the numerical solutions for 800, 1600 and 3200 cells with the exact solution for a Riemann problem with a SG EOS at $t = 0.1\ s$ ($CFL^+ = 0.015$).

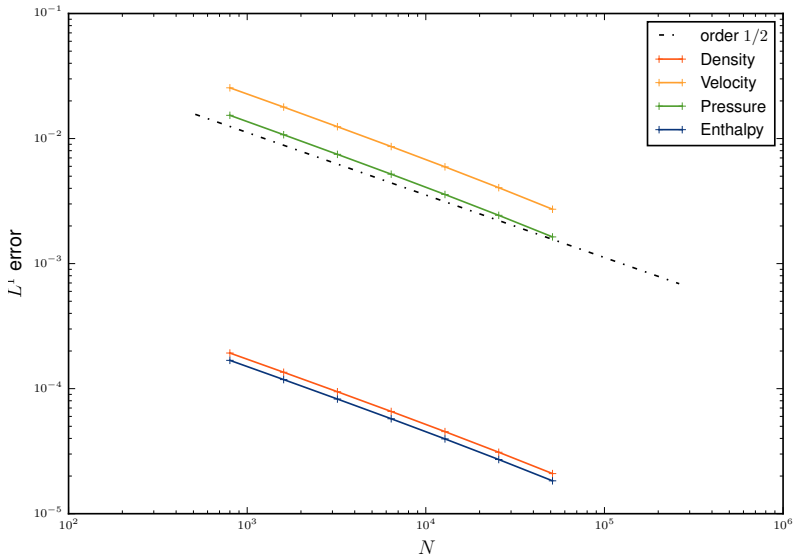

Figure 7: L^1 convergence curves for a Riemann problem with a SG EOS ($CFL^+ = 0.015$).

dx	N	ρ cnv. order	u cnv. order	P cnv. order	h cnv. order
5.0e-1	800				
2.5e-1	1600	0.5110	0.5120	0.5157	0.5107
1.25e-1	3200	0.5171	0.5209	0.5211	0.5168
6.25e-2	6400	0.5243	0.5274	0.5270	0.5240
3.125e-2	12800	0.5353	0.5389	0.5392	0.5349
1.5625e-2	25600	0.5486	0.5535	0.5536	0.5480
7.8125e-3	51200	0.5665	0.5731	0.5733	0.5658

Table 4: L^1 convergence order for variables (ρ, u, P, h) for all the considered meshes for a Riemann problem with a SG EOS ($CFL^+ = 0.015$).

Test case 2 with $CFL^+ = 1$

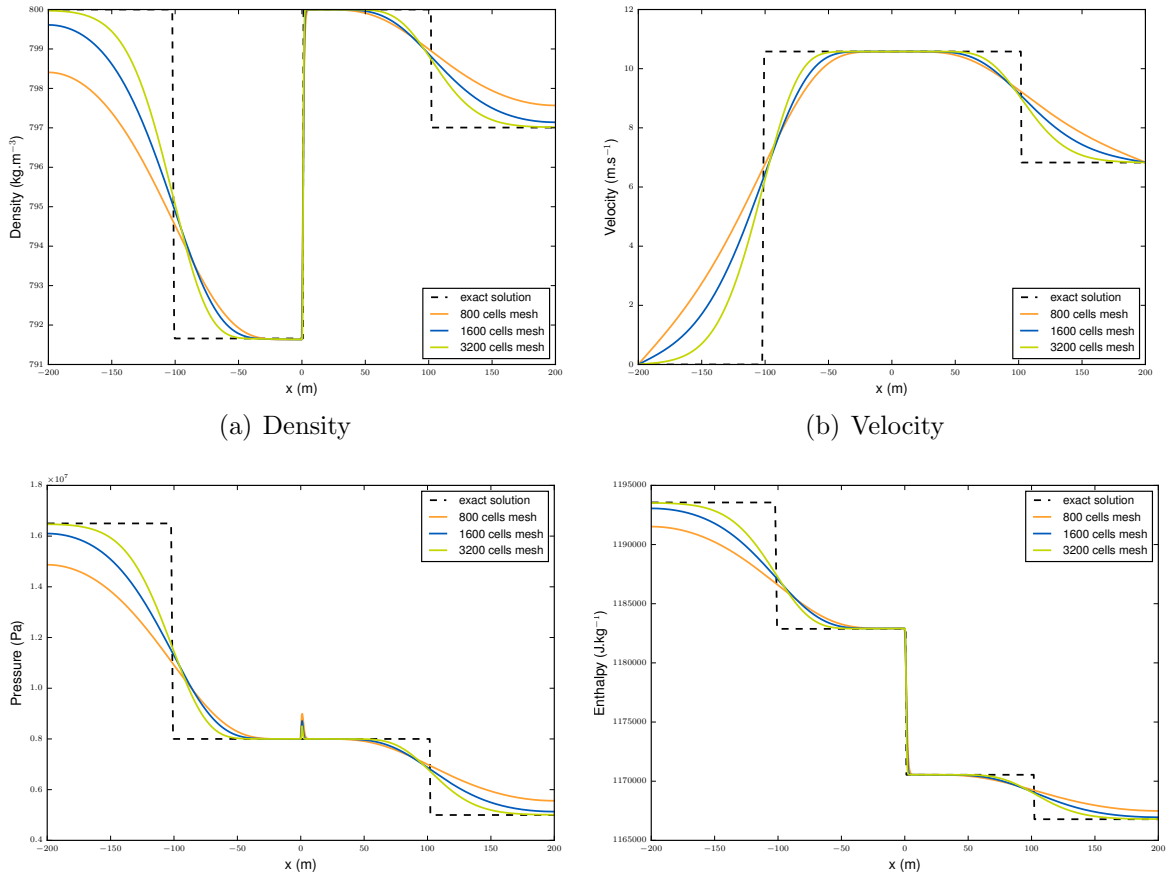

(a) Density (b) Velocity

(c) Pressure (d) Enthalpy

Figure 8: Comparison of the numerical solutions for 800, 1600 and 3200 cells with the exact solution for a Riemann problem with a SG EOS at $t = 0.1\ s$ ($CFL^+ = 1$).

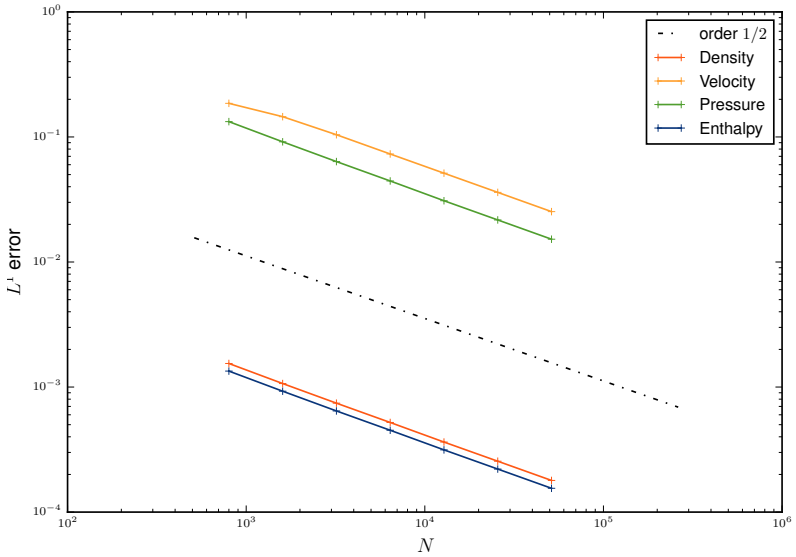

Figure 9: L^1 convergence curves for a Riemann problem with a SG EOS ($CFL^+ = 1$).

dx	N	ρ	u	P	h
5.0e-1	800	1.543e-03	1.857e-01	1.326e-01	1.342e-03
2.5e-1	1600	1.067e-03	1.453e-01	9.145e-02	9.263e-04
1.25e-1	3200	7.431e-04	1.042e-01	6.355e-02	6.440e-04
6.25e-2	6400	5.208e-04	7.307e-02	4.447e-02	4.512e-04
3.125e-2	12800	3.631e-04	5.132e-02	3.090e-02	3.144e-04
1.5625e-2	25600	2.552e-04	3.604e-02	2.169e-02	2.209e-04
7.8125e-3	51200	1.791e-04	2.528e-02	1.521e-02	1.550e-04

Table 5: L^1 error for variables (ρ, u, P, h) for all the considered meshes for a Riemann problem with a SG EOS ($CFL^+ = 1$).

dx	N	ρ cnv. order	u cnv. order	P cnv. order	h cnv. order
5.0e-1	800				
2.5e-1	1600	0.5327	0.3542	0.5364	0.5343
1.25e-1	3200	0.5214	0.4797	0.5250	0.5245
6.25e-2	6400	0.5129	0.5116	0.5149	0.5132
3.125e-2	12800	0.5202	0.5097	0.5253	0.5211
1.5625e-2	25600	0.5089	0.5010	0.5103	0.5094
7.8125e-3	51200	0.5108	0.5115	0.5118	0.5111

Table 6: L^1 convergence order for variables (ρ, u, P, h) for all the considered meshes for a Riemann problem with a SG EOS ($CFL^+ = 1$).

6.2. Verification test cases: one-dimensional shock tube interaction with a wall

The aim here is to simulate the interaction between a shock wave generated by a subsonic shock tube experiment and a wall. The shock tube experiment has been presented in the previous Section 6.1. In this second test case, the computational domain contains a

wall boundary on the right located at $x = x_1$; here, a wall boundary condition is applied. The 3-shock wave is reflected by the wall, and then the reflected shock interacts with the 2-contact discontinuity at time t_1 in $x = x^* = x_1 - \sigma_3(t_1 - t_0) = x_0 + u_1 t_1$, where t_0 denotes the time when the initial 3-shock wave hits the wall and u_1 and σ_3 the celerity of the contact discontinuity and the reflected shock wave respectively. The computed configurations are:

- the interaction of the initial shock wave with the wall,
- the interaction of the initial contact discontinuity with the reflected shock wave.

The localisation of the different constant fluid states is given in Figure 10. The state (3) is created by the shock wave reflection on the wall and the states (4) and (5) are created by the interaction of the contact discontinuity (1) and the reflected shock (3).

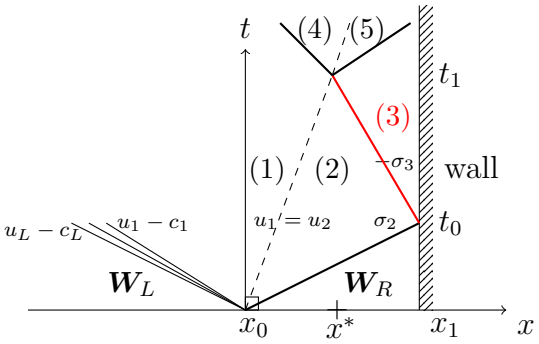

Figure 10: Wave interactions with the wall (subsonic case: $u_1 - c_1 < 0$).

Appendix C presents the calculation of the analytic solution (hence computing exact values for $\boldsymbol{W}_3$, $\boldsymbol{W}_4$ and $\boldsymbol{W}_5$) based on an exact solving of two distinct Riemann problems. In the following section, the numerical solution is compared with this analytic solution in order to check the numerical scheme error and to investigate convergence rates.

6.2.1. Interaction of the initial contact discontinuity with the reflected shock wave for an ideal gas EOS

The computational domain is initialized with the Sod shock-tube configuration. The discontinuity between the initial left and right states is located at $x_0 = 50\ m$. Initial conditions are:

$$\begin{cases} (\rho_L, u_L, P_L) = (1, 0, 10^5)\,, \\ (\rho_R, u_R, P_R) = (0.125, 0, 10^4)\,. \end{cases} \tag{44}$$

and: $P = (\gamma - 1)\,\rho\epsilon$, with $\gamma = \frac{7}{5}$.
The convergence study is performed with uniform meshes. The mesh contains N cells with $N = 800$, 1600, 3200, 6400, 12800, 25600 or 51200. The material CFL_u value is equal to 1. The computation final time is 0.42 s such that the reflected shock wave has interacted with the initial contact discontinuity. Numerical diffusion affects obtained profiles, but these latter are in quite good agreement with the exact solution (dark dashed line), see Figure 11 and Table 7. The L^1 convergence orders are close to 0.5 for the density, and close to 0.6 for the pressure and the velocity (see Figure 12 and Table 8). For $N = 12800$, the numerical wall pressure is $P_{wall}^{num} = 78038.0843\ Pa$ to be compared with the theoretical

value $P_{wall}^{exact} = 78038.3071\ Pa$ (arising from Appendix C). The relative error is 2.9×10^{-6}.

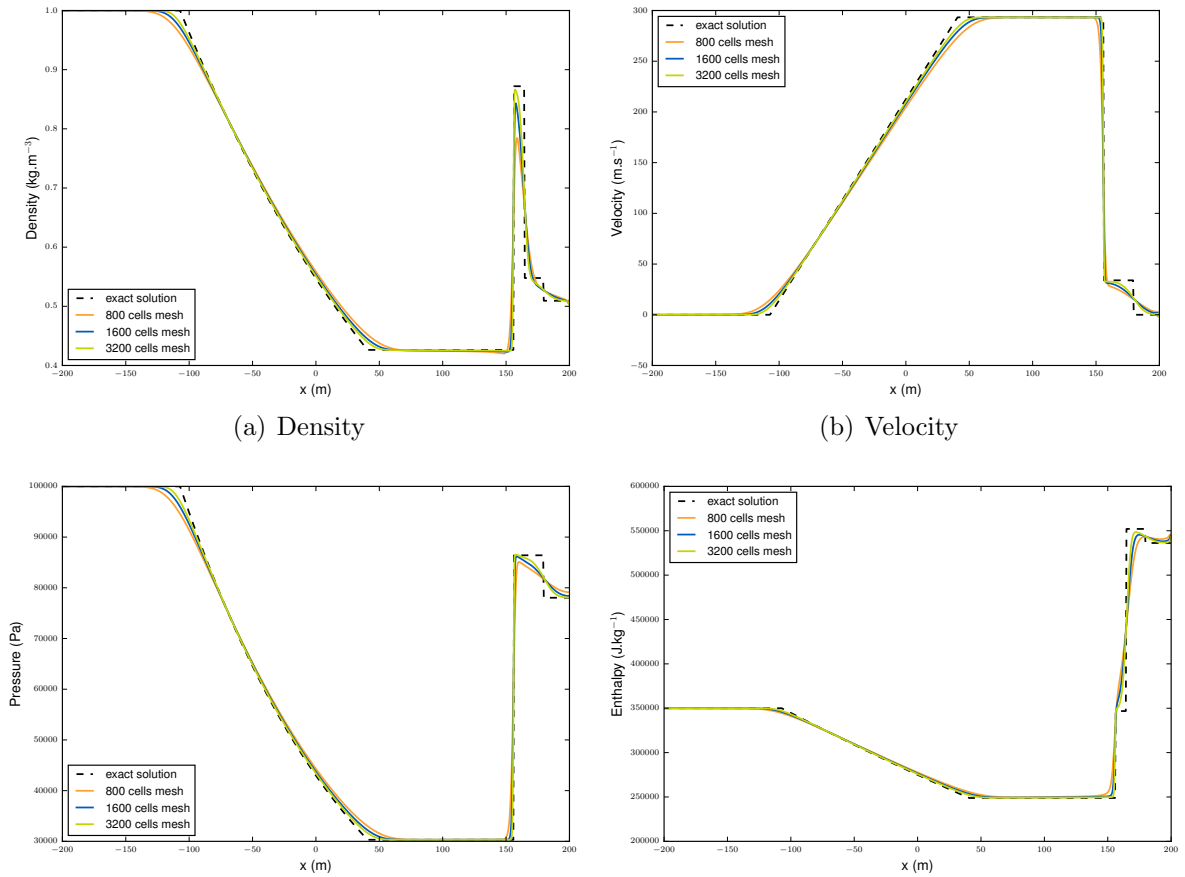

(a) Density (b) Velocity

(c) Pressure (d) Enthalpy

Figure 11: Comparison of the numerical solutions for 800, 1600 and 3200 cells with the exact solution for the Sod shock-tube interaction case at $t = 0.42\ s$.

dx	N	ρ	u	P	h
5.0e-1	800	5.143e-02	5.508e-02	3.673e-02	3.938e-02
2.5e-1	1600	3.680e-02	3.631e-02	2.332e-02	2.774e-02
1.25e-1	3200	2.562e-02	2.294e-02	1.468e-02	1.906e-02
6.25e-2	6400	1.781e-02	1.495e-02	9.649e-03	1.322e-02
3.125e-2	12800	1.209e-02	9.426e-03	6.181e-03	9.107e-03
1.5625e-2	25600	8.247e-03	6.062e-03	4.003e-03	6.290e-03
7.8125e-3	51200	5.569e-03	3.766e-03	2.507e-03	4.320e-03

Table 7: L^1 error for variables (ρ, u, P, h) for all the considered meshes for the Sod shock-tube interaction case.

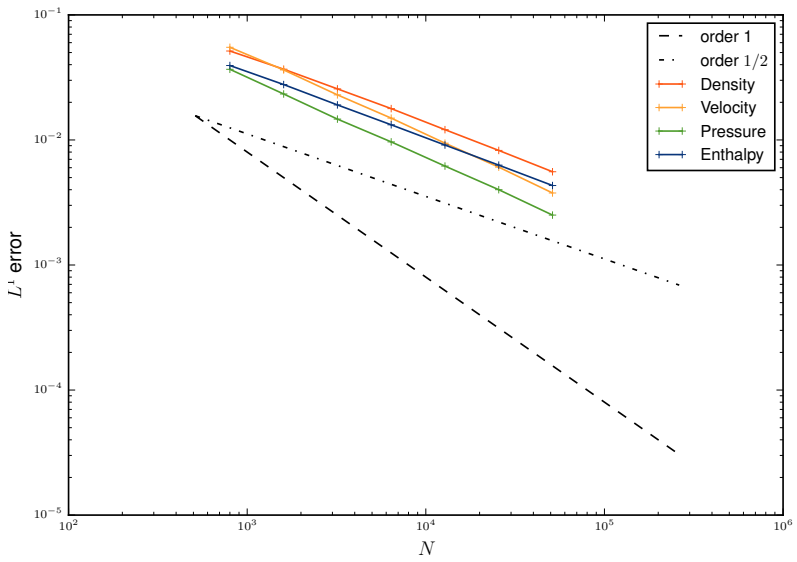

Figure 12: L^1 convergence curves of for Sod shock-tube interaction case.

dx	N	ρ cnv. order	u cnv. order	P cnv. order	h cnv. order
5.0e-1	800				
2.5e-1	1600	0.4829	0.6012	0.6557	0.5056
1.25e-1	3200	0.5226	0.6626	0.6671	0.5411
6.25e-2	6400	0.5244	0.6182	0.6057	0.5281
3.125e-2	12800	0.5594	0.6649	0.6427	0.5377
1.5625e-2	25600	0.5516	0.6368	0.6269	0.5338
7.8125e-3	51200	0.5663	0.6868	0.6748	0.5419

Table 8: L^1 convergence order for variables (ρ, u, P, h) for all the considered meshes for the Sod shock-tube interaction case.

6.2.2. Shock wave reflection on a wall for a stiffened gas EOS

The verification test case is still a shock tube experiment that interacts with a wall, now considering a stiffened gas EOS. The stiffened gas parameters are:

$$\gamma_{SG} = 5 \quad \text{and} \quad \Pi_\infty = 1.345951 \times 10^8 \ Pa.$$

The membrane is located at $x_0 = 50\ m$. Initial conditions are:

$$\begin{cases} (\rho_L, u_L, P_L) = (762.8, 0, 1.65 \times 10^7)\,, \\ (\rho_R, u_R, P_R) = (762.8, 0, 1.55 \times 10^7)\,. \end{cases} \tag{45}$$

This test case corresponds to a low Mach number flow. Indeed the Mach number varies from 0 to 10^{-3}. The convergence study is performed with the same uniform meshes. CFL_u is equal to 0.005 (*i.e.* $CFL_{u+c} \approx 5$). The CFL_u value is chosen small enough to capture accurately the shock wave profile. The computation final time is 0.21 s such that the reflected shock wave has been generated by interaction with the wall. The field values of the shock after the wall reflection fit the exact solution (see Figure 13 and Table 9). The expected L^1 convergence orders are recovered: approximately 0.5 for the density, the pressure and the velocity (see Figure 14 and Table 10). For $N = 12800$ cells, the

numerical wall pressure after the reflection on the wall is $P_{wall}^{num} = 16500348\ Pa$ to be compared with the theoretical value $P_{wall}^{exact} = 16500335\ Pa$ (arising from Appendix C). The relative error is 7.8×10^{-7}.

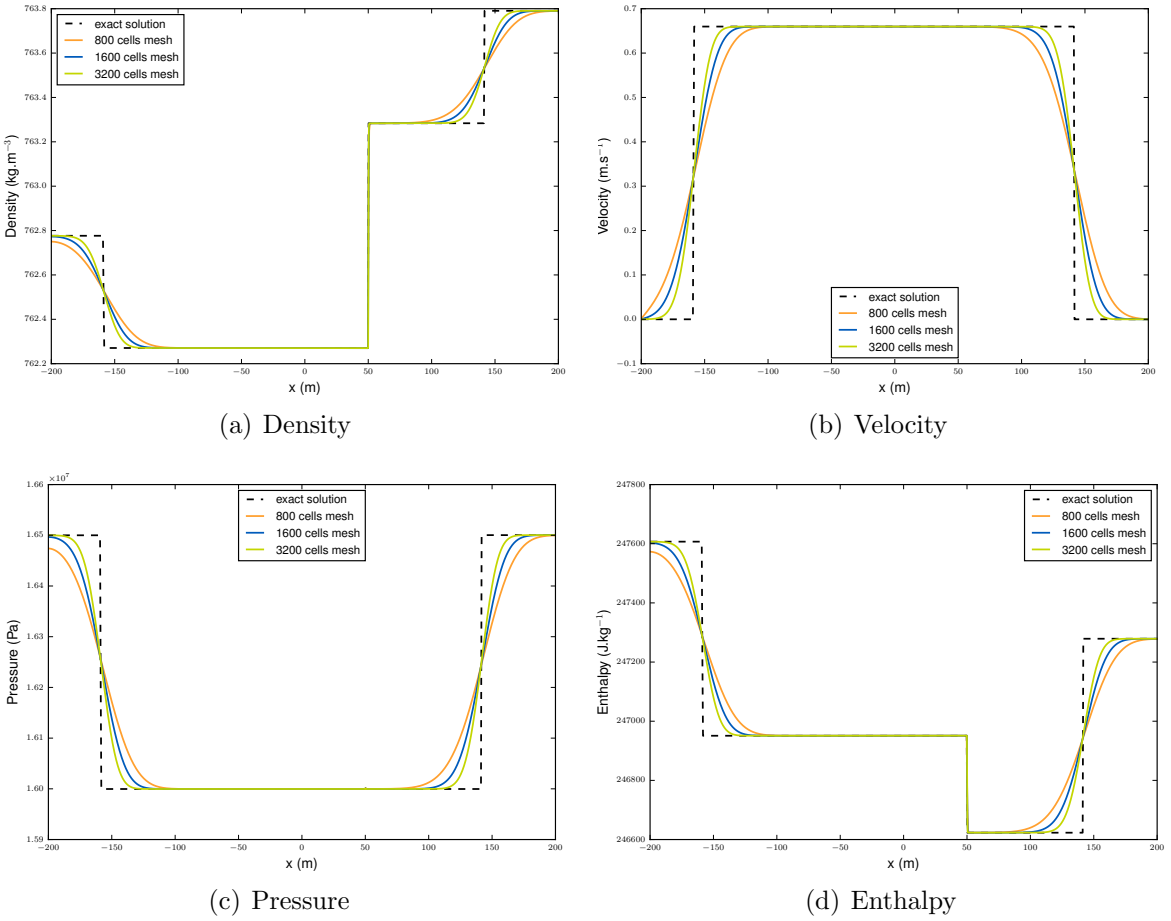

(a) Density (b) Velocity

(c) Pressure (d) Enthalpy

Figure 13: Comparison of the numerical solutions for 800, 1600 and 3200 cells with the exact solution for the shock-tube reflection case with a SG EOS at $t = 0.21\ s$.

dx	N	ρ	u	P	h
5.0e-1	800	5.401e-05	1.059e-01	2.504e-03	2.147e-04
2.5e-1	1600	3.857e-05	7.607e-02	1.776e-03	1.525e-04
1.25e-1	3200	2.714e-05	5.377e-02	1.253e-03	1.076e-04
6.25e-2	6400	1.915e-05	3.793e-02	8.840e-04	7.589e-05
3.125e-2	12800	1.351e-05	2.673e-02	6.230e-04	5.350e-05
1.5625e-2	25600	9.501e-06	1.880e-02	4.382e-04	3.763e-05
7.8125e-3	51200	6.668e-06	1.319e-02	3.075e-04	2.641e-05

Table 9: L^1 error for variables (ρ, u, P, h) for all considered meshes for the shock-tube reflection case with a SG EOS.

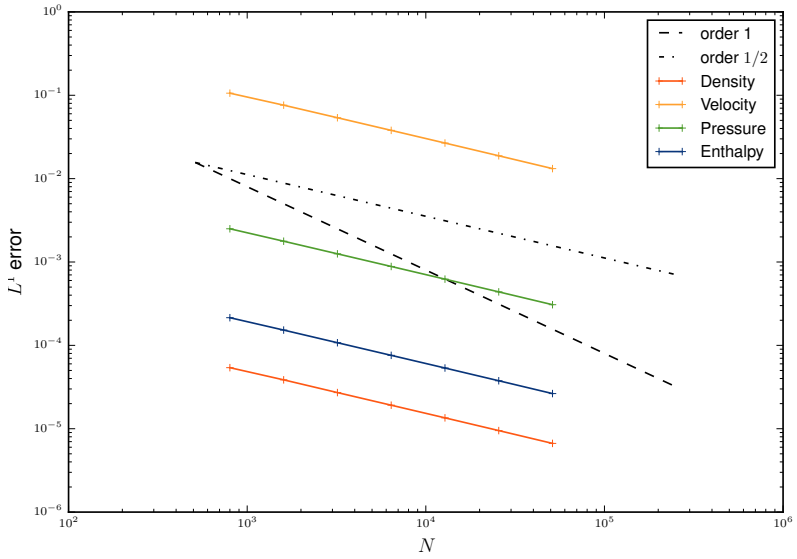

Figure 14: L^1 convergence curves for the shock-tube reflection case with a SG EOS.

dx	N	ρ cnv. order	u cnv. order	P cnv. order	h cnv. order
5.0e-1	800				
2.5e-1	1600	0.4855	0.4778	0.4958	0.4934
1.25e-1	3200	0.5073	0.5006	0.5025	0.5037
6.25e-2	6400	0.5028	0.5034	0.5037	0.5034
3.125e-2	12800	0.5040	0.5049	0.5047	0.5045
1.5625e-2	25600	0.5075	0.5078	0.5078	0.5077
7.8125e-3	51200	0.5107	0.5110	0.5110	0.5109

Table 10: L^1 convergence order for variables (ρ, u, P, h) for all considered meshes for the shock-tube reflection case with a SG EOS.

6.3. Integral formulation validation test case

EDF R&D has set up research programmes in order to investigate accidental situations in a major context of nuclear safety and security expertise for PWR (Pressurized Water Reactor) conditions, including RIA (Reactivity Initiated Accident) [2].

The aim of the current test case is to assess the integral formulation with obstacles, while mimicking the RIA situation. Thus, the numerical test case consists in simulating a fluid flow induced by the fuel during a RIA fast transient, where a shock wave impacts a fuel assembly, gathering a few rods. Actually, the desired physical quantity is the resultant pressure force on fuel rods in order to evaluate the mechanical properties of the rod cladding. Both the CFD fluid approach, where the mesh perfectly matches the rods, and the new integral approach, where fluid cells are obstructed by the rods, are used in this study. Results are thus compared to validate the integral approach. The CFD study provides the reference values.

6.3.1. Case description

The numerical test consists in a shock wave impacting rigid obstacles. The compressible fluid is assumed to be inviscid, and the flow is unsteady. The two-dimensional computational domain Ω is a large tube with a membrane in the middle which separates

two discontinuous constant fluid states $\boldsymbol{W}_L$ and $\boldsymbol{W}_R$ initially at rest. Both tube ends are closed by walls. Symmetry boundary conditions are imposed at the top and the bottom of the computational domain to enforce a periodic condition in the y-direction. An obstructed area composed of four solid rods is set on the right of the shock tube membrane. A sketch of the test case is displayed in Figure 15. The obstacles are squares of 1 cm edge. We perform several computations with Cartesian meshes:

- The reference $2D$ CFD computation using a fine fluid mesh including 87 millions of square cells, such that 2000 cells mesh the height h of the tube (see Figure 15).
- The integral formulation computations using coarse porous meshes with square cells. N_h cells mesh the height h of the tube: $N_h = \mathbf{1}$, 2, 3, 4, 5 or 6. Thus the obstructed pattern of size $h \times L/8$ is meshed with $3.5 \times N_h^2$ square cells (see Figure 15). The total number of cells in Ω is: $N_{cell} = 8 \times 3.5 \times N_h^2$.

The first mesh size ($N_h = \mathbf{1}$) is representative of the one used for a "component" computation with THYC or FLICA 4 codes for instance. Unlike with the CFD computation where the solid boundary is explicitly meshed (a wall boundary condition is enforced on the obstacle surface), the obstacles with the integral approach are included or partially included in the cells. The simulation is performed with a stiffened gas EOS modelling the liquid water thermodynamic in the PWR core. The stiffened gas parameters are:

$$\gamma_{SG} = 1.66512803 \quad \text{and} \quad \Pi_\infty = 3.7258761468 \times 10^8 Pa.$$

Initial conditions are, for left and right states:

$$\begin{cases} (\rho_L, u_L, P_L) = (713.187, 0, 200 \times 10^5)\,, \\ (\rho_R, u_R, P_R) = (729.614, 0, 155 \times 10^5)\,. \end{cases} \tag{46}$$

CFL^+ is equal to 0.006 (*i.e.* $CFL_{u+c} \approx 1$). The CFL^+ value is chosen small enough to capture accurately shock and rarefaction waves. The final time is 0.17 ms. Hence the fast waves (rarefaction and shock waves) do not hit the left and right wall boundaries. The CFD unsteady pressure field is plotted in Figure 16.

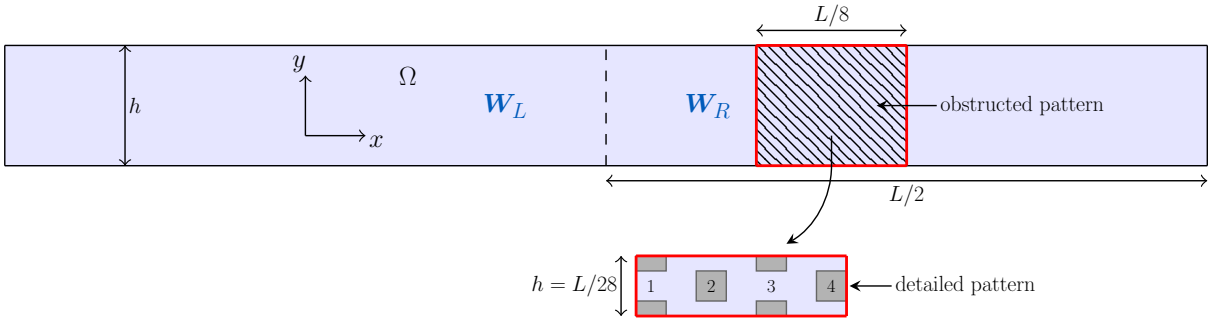

Figure 15: Sketch of the Ω domain of size $h \times L$ obstructed by four internal solid rods (in grey) and periodic in the y-direction. The pressure shock wave propagates from the middle of the domain towards the right end.

Note that explicit-in-time schemes, such as the one described in [21] would lower computational cost results for the same level of accuracy in this case, where the acoustic CFL_{u+c} number is close to one, in order to be accurate on pressure loads associated with fast waves. However this test case validates the ability of the semi-implicit algorithm to deal with unsteady situations involving sharp genuinely non-linear shocks.

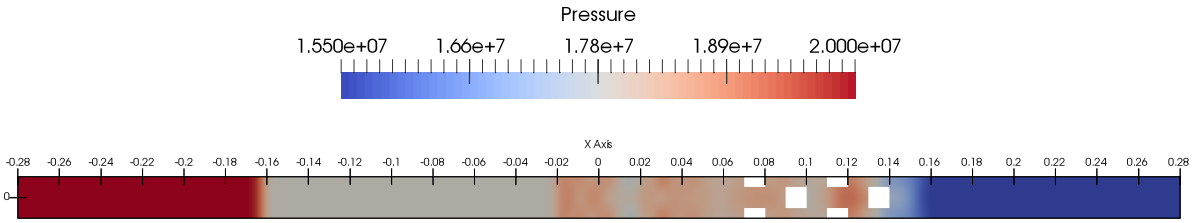

Figure 16: Pressure field obtained with the local CFD approach (870 000 cells), $t_{final} = 0.17\ ms$.

6.3.2. Numerical results

In order to validate the integral approach for the fluid variables, the unsteady profiles of the density, the x-velocity component and the pressure, for the coarse mesh integral approach computations, are compared, at $t_{final} = 0.17\ ms$, with the local CFD profiles in Figure 17. These one-dimensional profiles, along the x-direction, are obtained as a volume-average of the fluid fields in the y-direction. We retrieve the plateau values for the pressure, the velocity and the density for $x \in [-0.15, -0.05]$. These values are exactly those obtained when solving the one-dimensional Riemann problem associated with the current initial conditions (46). The profiles in the obstructed area, for $x \in [0.07, 0.14]$, give satisfactory profiles for the fluid variables, when compared with the CFD reference.

In order to compare the integral approach and the local approach on the quantity of interest, the pressure force exerted by the pressure shock wave on the surface of the four rods is computed from the numerical simulations with both the integral approach and the CFD reference simulation. Figure 18 presents a mesh refinement study for the pressure force using several meshes ($N_{cell} = 87 \times 10^4$, 3.48×10^6, 13.92×10^6 or 87×10^6). The maximal relative difference between the finest and the coarsest CFD mesh is 14%. The finest CFD computation with $N_{cell} = 87 \times 10^6$ is the reference.

The x-component of the pressure force $F_x(t)$ is defined as:

$$F_x(t) = \left(\int_{\Gamma^w} P(\mathbf{x}, t)\ \boldsymbol{n} \mathrm{d}\Gamma \right) \cdot \boldsymbol{e}_x,$$

where for the integral approach $P(\mathbf{x}, t^n)|_{\Gamma^w}$ is equal to P_i^n for all wall interfaces in the cell Ω_i, according to the 0^{th}-order approximation (24). For each mesh, the pressure force as a function of time $F_x(t)$ is plotted in Figure 19; in addition the time integral of the force, called impulsion, as a function of time is given in Figure 20. The impulsion is defined as:

$$J_x(t) = \int_0^t F_x(\tau) d\tau.$$

The results reveal that:

- For all computations, the maximal resultant force with the integral approach is underestimated for the rods 1, 2, 3, 4 and their sum, when compared with the CFD reference; however the resultant force with the integral approach has the same order of magnitude as the one with the CFD reference. Note that the maximal value of the sum of the forces exerted on the rods is less underestimated than the one exerted rod by rod, see Figure 19. Besides, we observe that the convergence towards the CFD reference computation is not monotonous for coarse porous meshes.

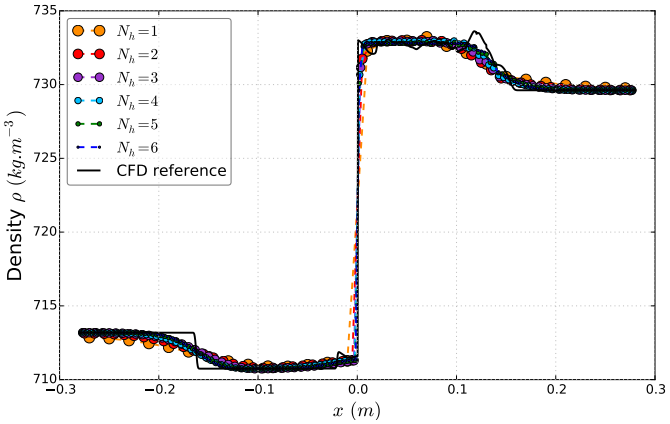

(a) Density

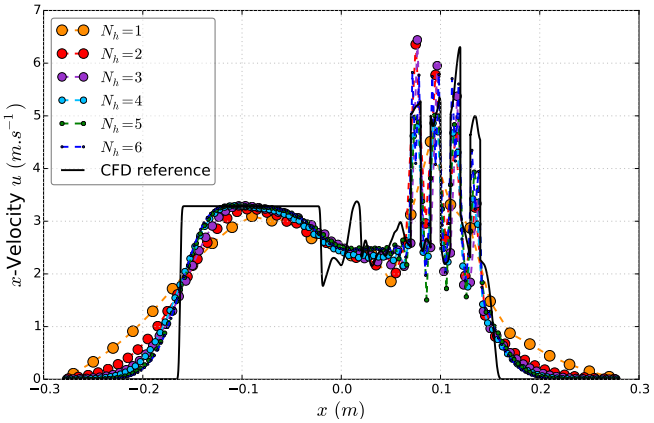

(b) x-Velocity

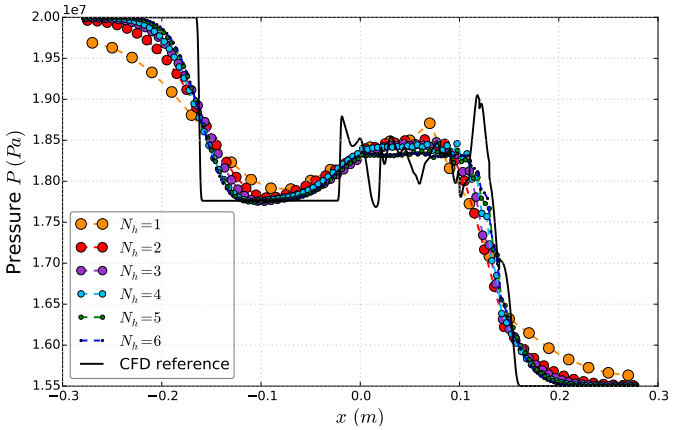

(c) Pressure

Figure 17: Fluid fields, at $t_{final} = 0.17\ ms$, averaged in the y-direction using the **integral** approach with different **coarse** meshes – comparison with the CFD reference (black line).

- The impulsion approximation on the coarse meshes is slightly overestimated for all computations when compared with the CFD reference, see Figure 20.
- As expected, Figure 21 shows that the integral approach converges towards the CFD approach when refining the mesh.

- Figure 22 and 23 show the quantities of interest (force and impulsion) computed with the 1^{st}-order approximation (26) of the wall pressure in the algorithm, and using the post-treatment: $P(\mathbf{x},t)|_{\Gamma^w} = P_i + \rho_i c_i \mathbf{u}_i \cdot \boldsymbol{n}$ on the wall boundary of the cell Ω_i. The latter values are actually different from those obtained with the 0^{th}-order approximation on very coarse meshes (see Figure 24); as expected, they are almost identical on very fine meshes, since $\mathbf{u}_i \cdot \boldsymbol{n}$ tends to zero close to the wall. Moreover, when compared with the CFD reference, the maximal value of the sum of the forces exerted on the rods and the impulsion, using the 1^{st}-order approximation (26), are overestimated on very coarse meshes.

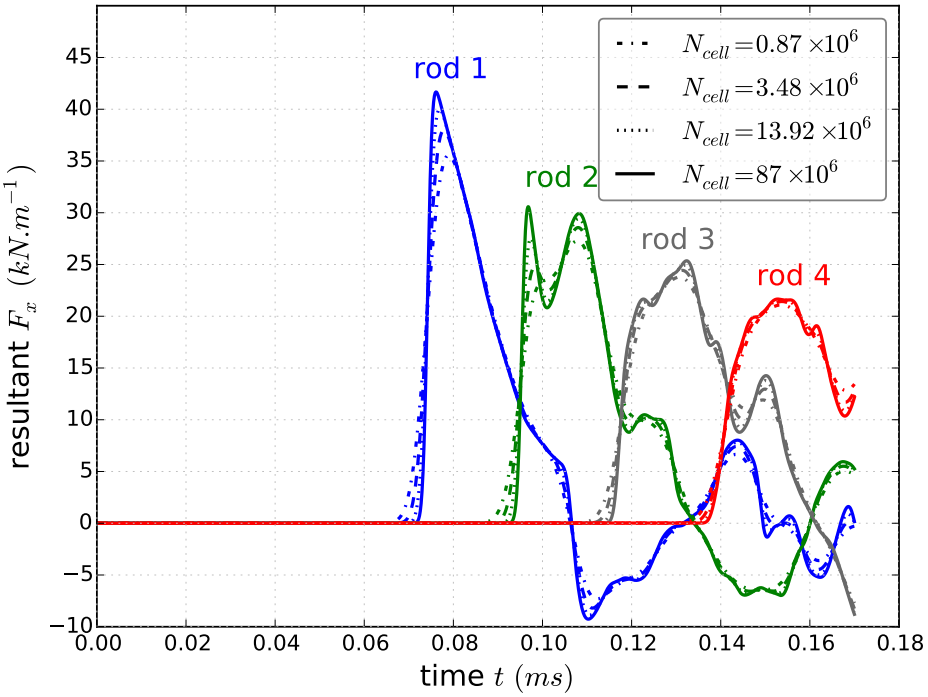

Figure 18: Resultant pressure force $F_x(t)$ using different meshes with N_{cell} cells – **CFD** approach.

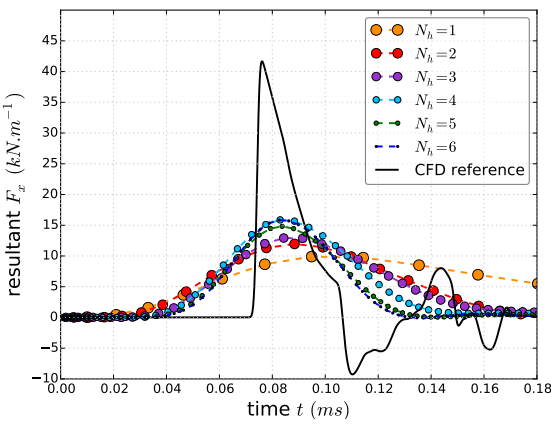

(a) Rod 1

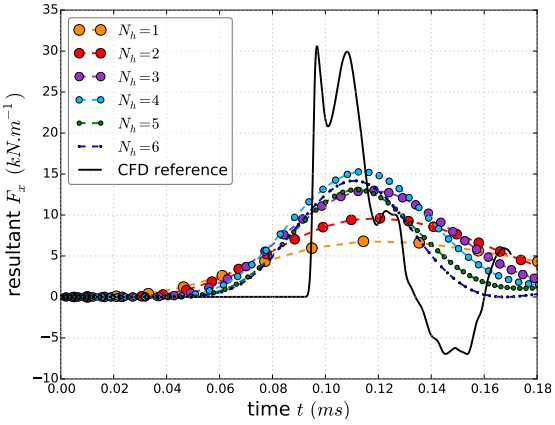

(b) Rod 2

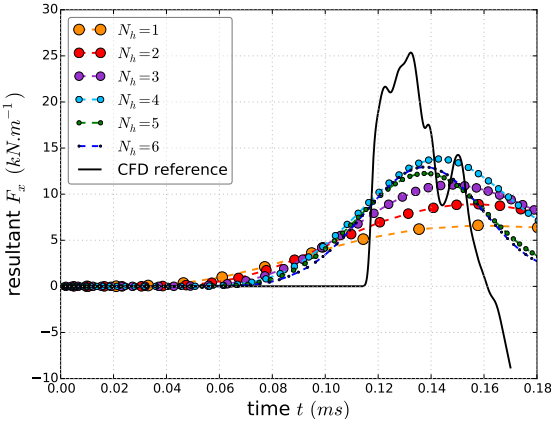

(c) Rod 3

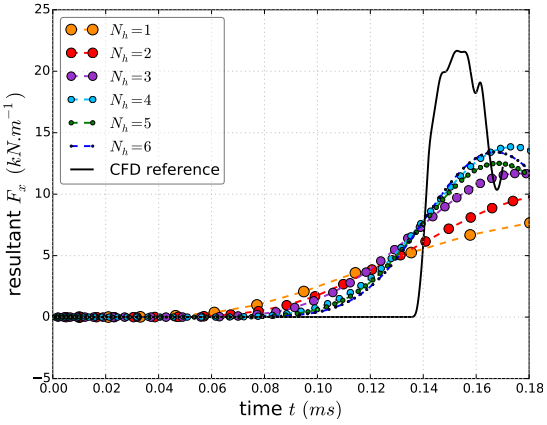

(d) Rod 4

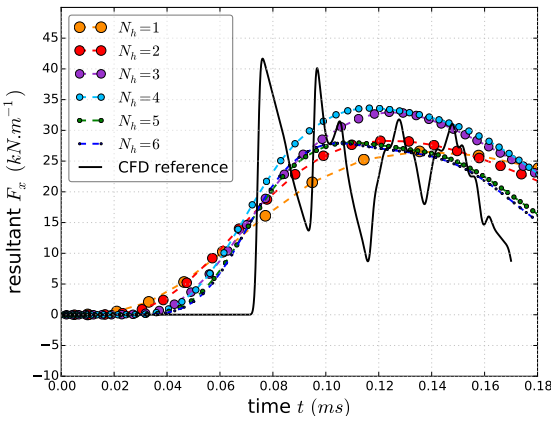

(e) Rods sum

Figure 19: Resultant pressure force $F_x(t)$ using the **integral** approach with different **coarse** meshes – comparison with the CFD reference (black line).

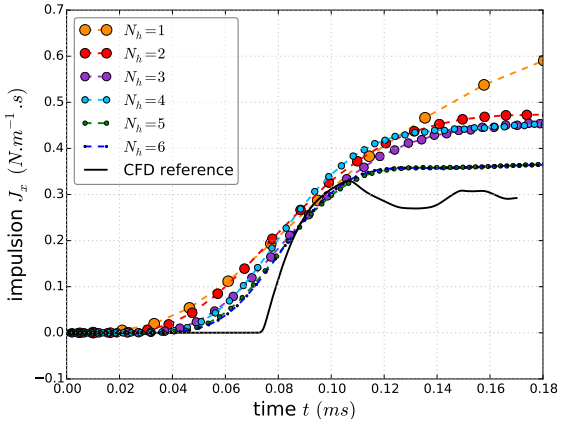

(a) Rod 1

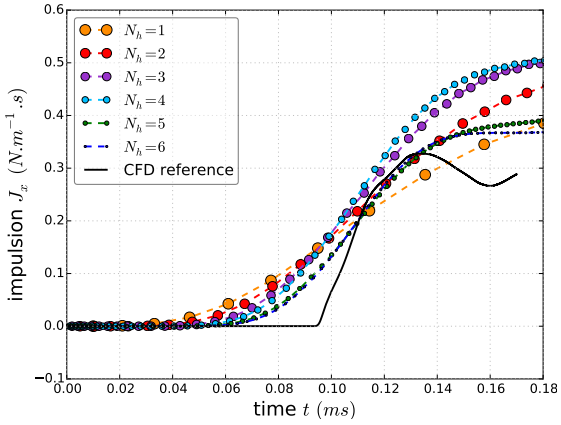

(b) Rod 2

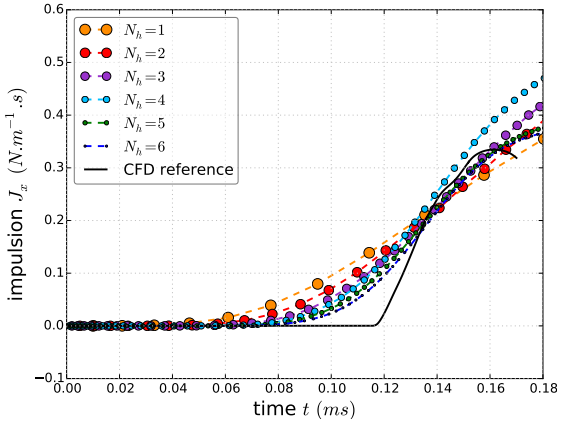

(c) Rod 3

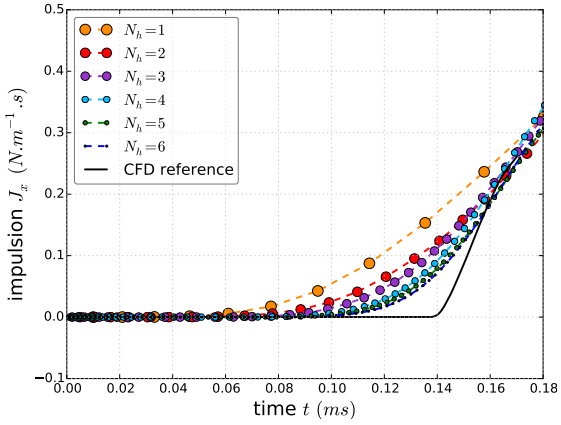

(d) Rod 4

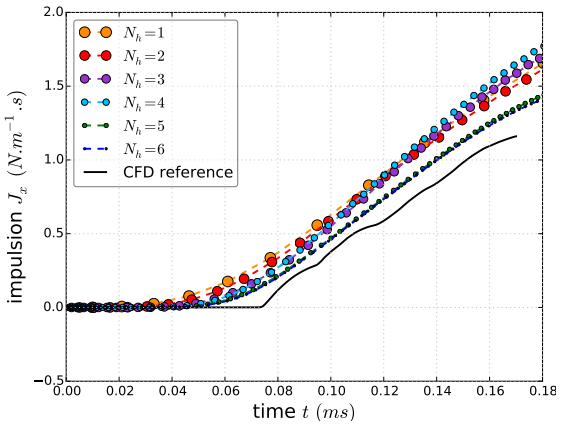

(e) Rods sum

Figure 20: Pressure force impulsion $J_x(t)$ using the **integral** approach with different **coarse** meshes – comparison with the CFD reference (black line).

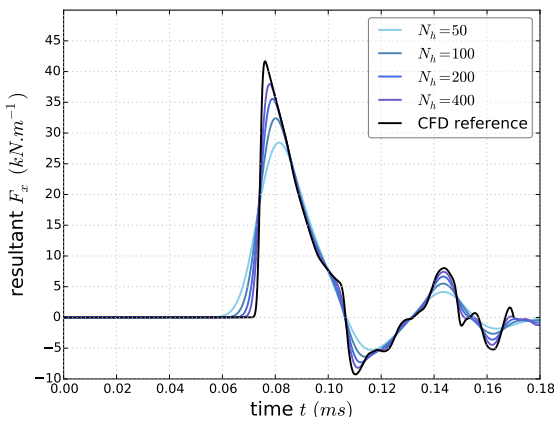

(a) Rod 1

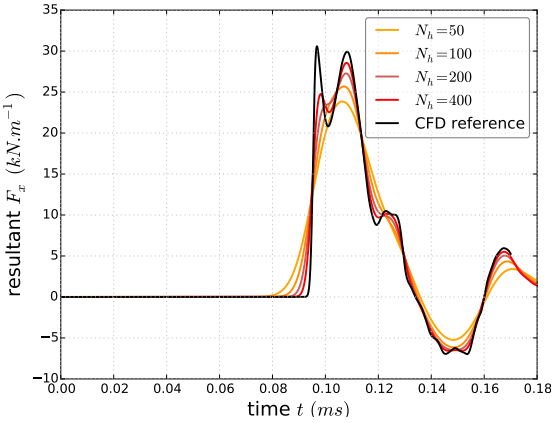

(b) Rod 2

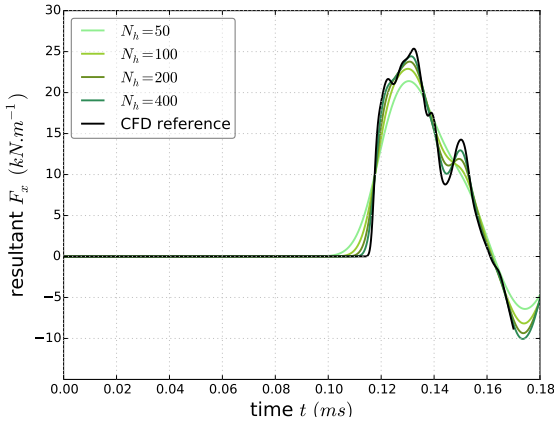

(c) Rod 3

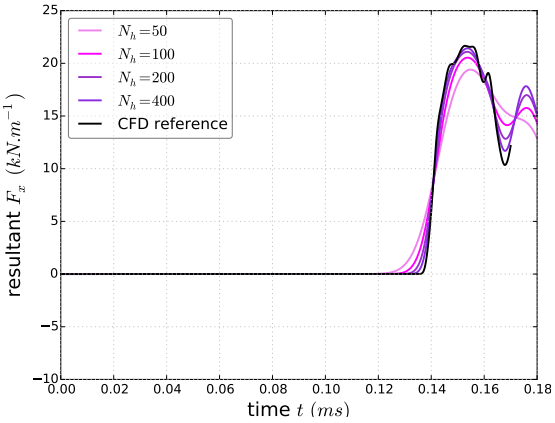

(d) Rod 4

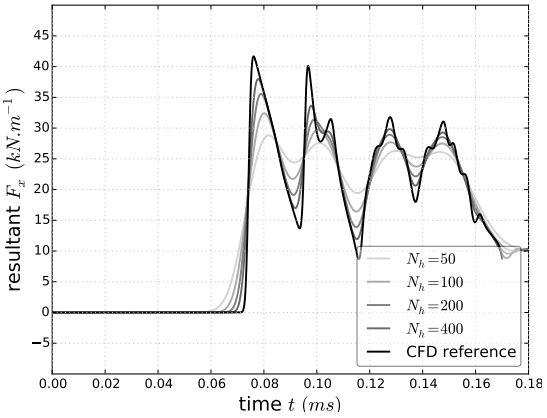

(e) Rods sum

Figure 21: Resultant pressure force $F_x(t)$ using the **integral** approach with different **fine** meshes – comparison with the CFD reference (black line).

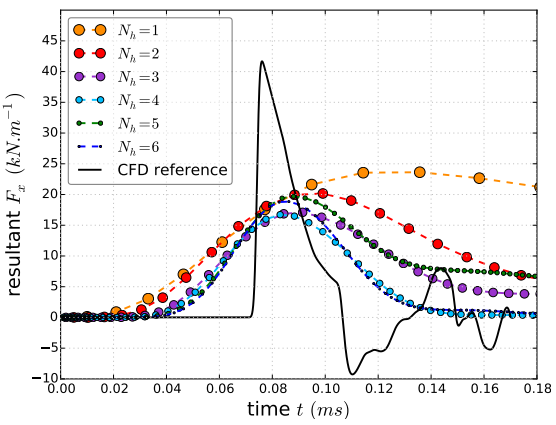

(a) Rod 1

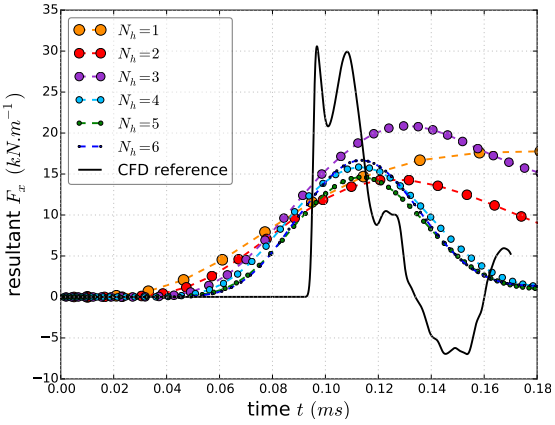

(b) Rod 2

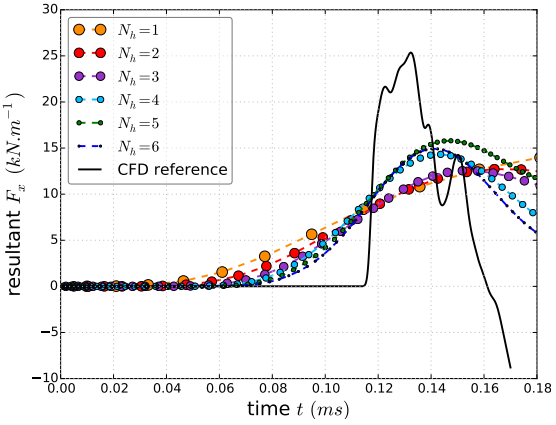

(c) Rod 3

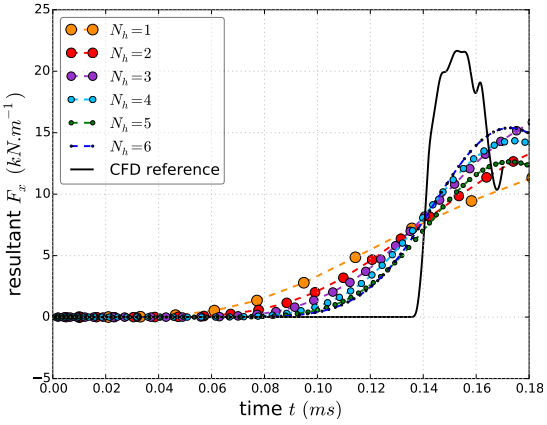

(d) Rod 4

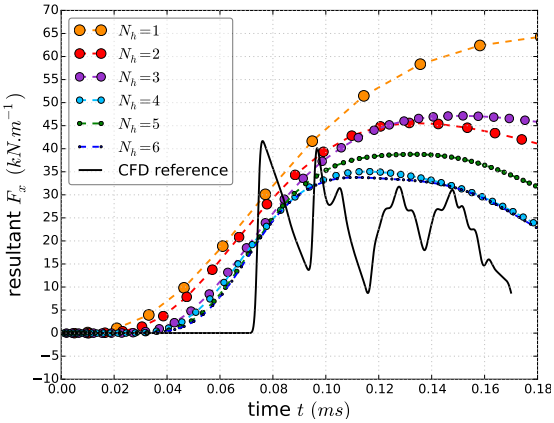

(e) Rods sum

Figure 22: Resultant pressure force $F_x(t)$ using the **integral** approach with different **coarse** meshes and **the 1^{st}-order approximation** of the wall pressure – comparison with the CFD reference (black line).

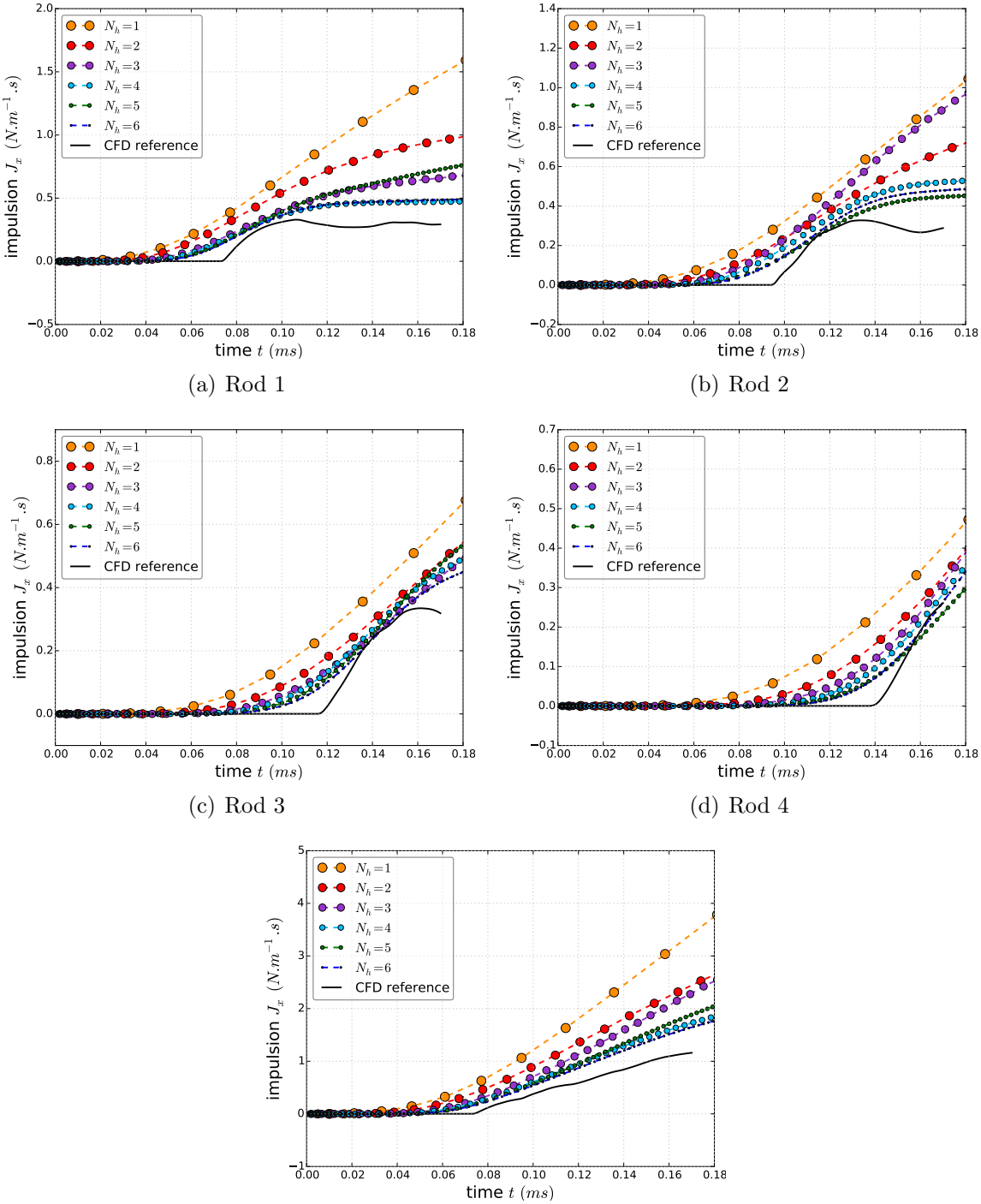

(a) Rod 1

(b) Rod 2

(c) Rod 3

(d) Rod 4

(e) Rods sum

Figure 23: Pressure force impulsion $J_x(t)$ using the **integral** approach with different **coarse** meshes and **the 1^{st}-order approximation** of the wall pressure – comparison with the CFD reference (black line).

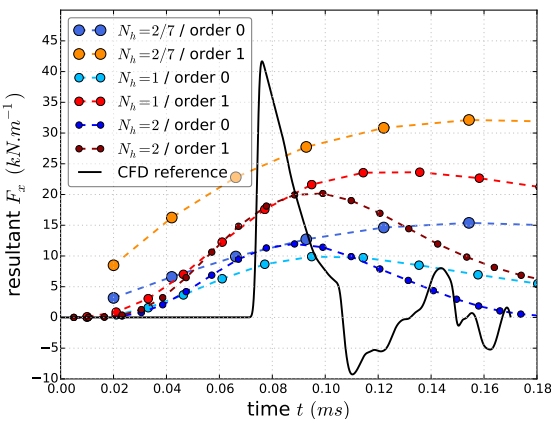

(a) Rod 1

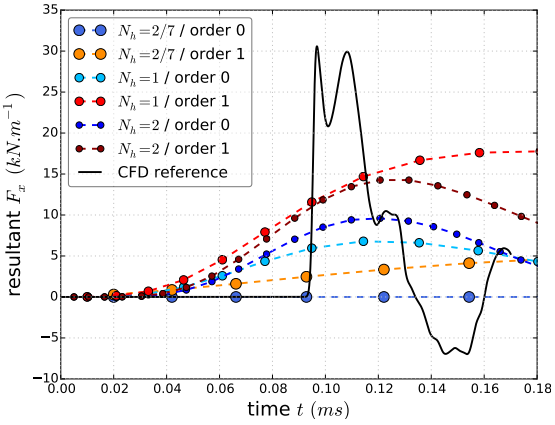

(b) Rod 2

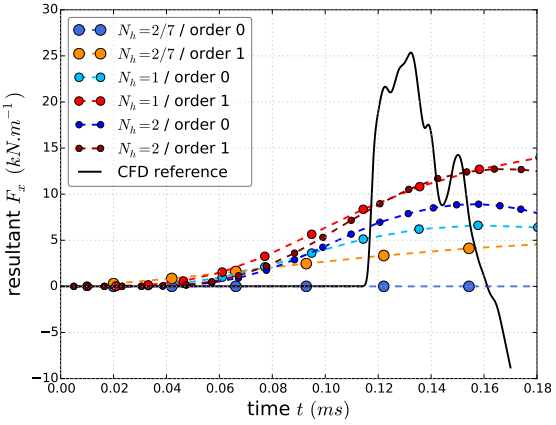

(c) Rod 3

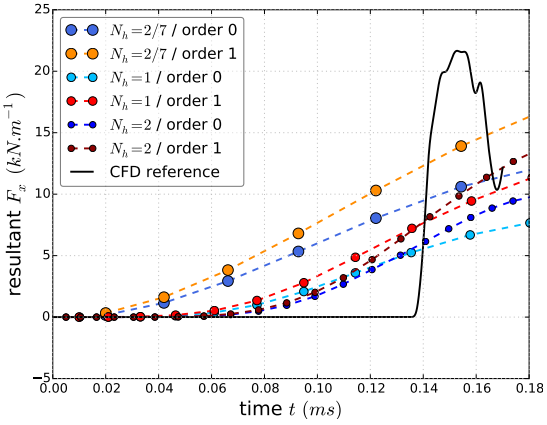

(d) Rod 4

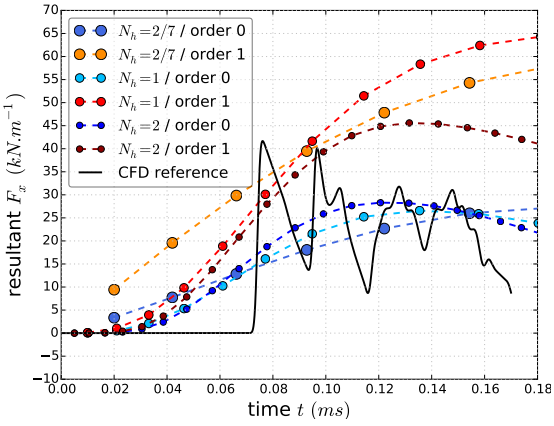

(e) Rods sum

Figure 24: Resultant pressure force $F_x(t)$ using the **integral** approach with three **very coarse** meshes – **comparison of the 0^{th}-order approximation with the 1^{st}-order approximation** of the wall pressure.

7. Conclusion

The multi-dimensional integral formulation has been introduced to approximate solutions of the Euler equations in a domain cluttered up by small solid obstacles compared with the global size of the domain. Thus, the obstacles may not be explicitly meshed in the computational domain. The integral formulation uses an original pressure-correction method in a co-located semi-implicit finite volume conservative scheme. The preservation of the positivity of the density and the internal energy under a CFL condition, based on the material velocity, is proved.

Numerical verification tests presented herein are shock tube problems, for gas or liquid, either in a free domain or in a domain closed by a wall reflecting the incident shock wave. These tests indicate a stable and consistent behaviour of the algorithm, for Mach numbers ranging from 10^{-3} to 1. Indeed, the numerical scheme enables to capture correct shock waves and contact discontinuities, and also to reproduce the correct pressure, density and velocity profiles in rarefaction waves. We emphasize that the numerical rate of convergence is similar to those obtained with classical exact or approximate Riemann solvers.

The numerical validation test, representative of a safety industrial experiment, shows the ability of the integral approach, with porous coarse meshes, to obtain integral quantities, such that forces acting on tube bundles, with the same order of magnitude than the fine CFD solution. The zero and the first order approximation of the wall pressure in the integral approach are tested. Furthermore, the integral approach naturally converges towards the CFD approach when the mesh is refined.

Hence, by simply defining mesh geometric quantities like fluid volumes and fluid surfaces, the integral formulation allows to unify the porous and the fluid representation by construction. Thus a wide range of computational meshes, from the coarsest porous mesh for the "component" scale to the finest fluid mesh for the "local" scale, can be continuously treated. The current integral approach is an alternative to the standard porous approach in order to compute fluid flows in an obstructed medium, including the sharp transition between a free and an obstructed medium, as it occurs when the fluid flow enters the PWR core. Numerical tests involving comparisons with results performed with the component scale software THYC, using the standard porous approach, will be carried out in the near future.

Current work aims at extending the integral formulation to compressible and incompressible viscous fluid flows governed by the Navier-Stokes equations. Viscous effects would be taken into account thanks to wall functions which vanish when the mesh is refined.

Acknowledgments The first author receives a financial support by ANRT through an EDF-CIFRE contract 2016/0728. All computational facilities were provided by EDF R&D. This work has benefited from fruitful discussions with Prof. T. Gallouët and Prof. R. Herbin (Aix-Marseille Université).

Appendix A. Mass balance non linear scheme for liquid

The mass balance step of the pressure-correction algorithm (see Section 3.1) is modified for a real Equation Of State (EOS) of a liquid.

Appendix A.1. Time scheme

At the time step Δt^n, pressure and density are implicit, while entropy is always considered frozen, $s^{n+1} = s^n$. Integration of the mass balance equation between t^n and t^{n+1} and over Ω_i^ϕ gives the following implicit time scheme:

$$\left|\Omega_i^\phi\right| \left(\rho_i^{n+1} - \rho_i^n\right) + \Delta t^n \int_{\Gamma_i^\phi} \boldsymbol{Q}^* \cdot \boldsymbol{n} \mathrm{d}\Gamma = 0, \tag{A.1}$$

where the implicit mass flux $\boldsymbol{Q}^*$ is computed as (see Equation (13)):

$$\boldsymbol{Q}^* \cdot \boldsymbol{n} = \boldsymbol{Q}^n \cdot \boldsymbol{n} - \Delta t^n \boldsymbol{\nabla} P^* \cdot \boldsymbol{n}.$$

The relation between pressure and density is henceforth non linear: $\rho_i^{n+1} = \rho(P_i^*, s_i^n)$. Equation (A.1) is written with the unknown pressure P_i^* as follows:

$$\left|\Omega_i^\phi\right| \left(\frac{\rho(P_i^*, s_i^n)}{P_i^*} - (\Delta t^n)^2 \nabla \cdot \boldsymbol{\nabla}\right) P_i^* = \left|\Omega_i^\phi\right| \rho_i^n - \Delta t^n \int_{\Gamma_i^\phi} \boldsymbol{Q}^n \cdot \boldsymbol{n} \mathrm{d}\Gamma. \tag{A.2}$$

Remark Appendix A.1. *The relation $\rho_i^{n+1} = \rho\left(P_i^*, s_i^n\right)$ must be used for the update of the density to conserve mass over time.*

Appendix A.2. Space scheme

The space discretization of the mass balance equation (A.2) is identical to the scheme described in Section 4.1. The explicit mass flux is discretized by an upwind scheme:

$$\int_{\Gamma_i^\phi} \boldsymbol{Q}^n \cdot \boldsymbol{n} \mathrm{d}\Gamma = \sum_{j \in V(i)} \left(\rho_{ij}^n\right)^{upw} \left(\mathbf{u}^n \cdot \boldsymbol{n}\right)_{ij} S_{ij}^\phi, \tag{A.3}$$

with:

$$\left(\rho_{ij}^n\right)^{upw} = \beta_{ij}^n \rho_i^n + (1 - \beta_{ij}^n)\rho_j^n, \quad \beta_{ij}^n = \begin{cases} 1 & \text{if } \left(\mathbf{u}^n \cdot \boldsymbol{n}\right)_{ij} \geq 0, \\ 0 & \text{otherwise,} \end{cases}$$

and the pressure gradient is discretized with a two-point flux approximation:

$$\int_{\Gamma_i^\phi} \boldsymbol{\nabla} P^* \cdot \boldsymbol{n} \mathrm{d}\Gamma = \sum_{j \in V(i)} \frac{1}{h_{ij} + h_{ji}} \left(P_j^* - P_i^*\right) S_{ij}^\phi. \tag{A.4}$$

Thus the pressure prediction scheme holds:

$$\begin{aligned} \left|\Omega_i^\phi\right| \left(\frac{\rho(P_i^*, s_i^n)}{P_i^*}\right) P_i^* - (\Delta t^n)^2 \sum_{j \in V(i)} \frac{1}{h_{ij} + h_{ji}} \left(P_j^* - P_i^*\right) S_{ij}^\phi \\ = \left|\Omega_i^\phi\right| \rho_i^n - \Delta t^n \sum_{j \in V(i)} \left(\rho_{ij}^n\right)^{upw} \left(\mathbf{u}^n \cdot \boldsymbol{n}\right)_{ij} S_{ij}^\phi. \end{aligned} \tag{A.5}$$

Equation (A.5) yields a non-linear algebraic system:

$$\mathbf{M}\,\mathbf{X} = \mathbf{B}',$$

with the vector $\mathbf{X} = (P_i^*)_{i\in\{1,\dots,N_{cell}\}}$ and N_{cell} the total number of cell (or degrees of freedom). $\forall\, i \in \{1, ..., N_{cell}\}$, the diagonal operator coefficients are:

$$M_{ii} = \begin{cases} \left|\Omega_i^\phi\right| \left(\dfrac{\rho(P_i^*, s_i^n)}{P_i^*}\right) + (\Delta t^n)^2 \displaystyle\sum_{j\in V(i)} \frac{S_{ij}^\phi}{h_{ij}+h_{ji}} & \text{if } \left|\Omega_i^\phi\right| > 0, \\ 1 & \text{otherwise.} \end{cases}$$

$\forall\, i, j \in \{1, ..., N_{cell}\}$ with $j \neq i$, the off-diagonal coefficients are:

$$M_{ij} = \begin{cases} -\dfrac{(\Delta t^n)^2}{h_{ij}+h_{ji}} S_{ij}^\phi & \text{if } j \in V(i) \text{ and } \left|\Omega_i^\phi\right| > 0, \\ 0 & \text{otherwise.} \end{cases}$$

The right hand side coefficients are:

$$B_i' = \begin{cases} \left|\Omega_i^\phi\right| \rho_i^n - \Delta t^n \displaystyle\sum_{j\in V(i)} \left(\rho_{ij}^n\right)^{upw} (\mathbf{u}^n \cdot \boldsymbol{n})_{ij} S_{ij}^\phi & \text{if } \left|\Omega_i^\phi\right| > 0, \\ P_i^n & \text{otherwise.} \end{cases}$$

Appendix A.3. Property of positivity

The non linear operator $\mathbf{M}$ is coercive (therefore invertible) if the pressure is positive, *i.e.* for all i, $P_i^* \geq 0$. The sufficient condition of positivity of both the pressure and the density is the classical CFL-like condition (A.6) only based on the mass flux rather than the thermodynamic coefficient $\hat{\gamma} = \frac{\rho c^2}{P} > 1$.

Property Appendix A.1 (Positivity of the density and the pressure). *If the initial conditions are such that $\rho_i^n > 0$ and $P_i^n > 0$, then the density ρ_i^{n+1} and the pressure P_i^* will remain positive for all i, provided that the time step Δt^n complies with the CFL-like condition (A.6):*

$$\left|\Omega_i^\phi\right| \geq \Delta t^n \sum_{j\in V(i)} \beta_{ij}^n \left(\mathbf{u}^n \cdot \boldsymbol{n}\right)_{ij} S_{ij}^\phi. \tag{A.6}$$

Proof. The proof is similar to the proof of Property 5.1 in Section 5. The inverse operator $\mathbf{M}^{-1}$ is positive ($M_{ij}^{-1} \geq 0$) and the right hand side vector $\mathbf{B}'$ is also positive ($B_i' \geq 0$) if Condition (A.6) holds, implying $P_i^* \geq 0$. Besides, density ρ_i^{n+1} is computed as a positive function of the pressure $\rho_i^{n+1} = \rho\left(P_i^*, s_i^n\right) \geq 0$, which completes the proof.

Appendix B. Riemann problem with mirror state

A popular method to treat numerically solid wall boundary conditions is the "mirror state" technique. It consists in defining a virtual state $\widehat{\mathbf{W}}_i^n$ outside the multidimensional fluid domain, which is deduced from the state $\mathbf{W}_i^n$ in the nearest wall cell with the same density, pressure, but opposite normal velocity. The half Riemann problem consists in solving an exact one-dimensional Riemann problem with respect to this virtual state in the normal direction to the wall (see Figure B.25).

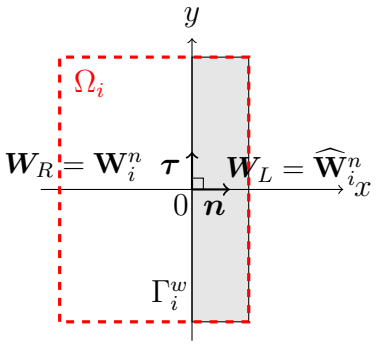

Figure B.25: Riemann problem with mirror state in the immersed obstacle into the cell Ω_i.

This problem is used to compute the wall pressure with *a priori* any EOS where $\boldsymbol{n}$ is the outward normal from the cell to the wall and $\boldsymbol{\tau}$ a tangent vector to the wall. Since Euler system (1) is invariant under frame rotation and translation along the $\boldsymbol{\tau}$ direction, the wall pressure is the solution of the local one-dimensional Riemann problem (B.1) in the $\boldsymbol{n}$-direction:

$$\begin{cases} \partial_t \boldsymbol{W} + \partial_{\boldsymbol{n}} \left(\boldsymbol{F}_{\boldsymbol{n}} \left(\boldsymbol{W} \right) \right) = 0, \ \boldsymbol{x} \cdot \boldsymbol{n} \in \mathbb{R}, \ t \in \mathbb{R}^+, \\ \boldsymbol{W}(\boldsymbol{x} \cdot \boldsymbol{n}, 0) = \begin{cases} \boldsymbol{W}_L & \text{if } \boldsymbol{x} \cdot \boldsymbol{n} < 0, \\ \boldsymbol{W}_R & \text{if } \boldsymbol{x} \cdot \boldsymbol{n} > 0, \end{cases} \end{cases} \tag{B.1}$$

where the left state $\boldsymbol{W}_L$ and the right state $\boldsymbol{W}_R$ are such that:

$$\begin{cases} \boldsymbol{W}_L = \mathbf{W}_i^n & \text{(real cell } i\text{)}, \\ \boldsymbol{W}_R = \widehat{\mathbf{W}}_i^n & \text{(virtual cell, mirror of } \mathbf{W}_i^n\text{)}, \end{cases} \tag{B.2}$$

and $\boldsymbol{F}_n(\boldsymbol{W}) = \boldsymbol{F}(\boldsymbol{W}) \cdot \boldsymbol{n}$ is the normal flux. For the two-dimensional Euler system:

$$\boldsymbol{W} = \begin{bmatrix} \rho \\ \rho \boldsymbol{u} \\ E \end{bmatrix} \text{ and } \boldsymbol{F}_n(\boldsymbol{W}) = \begin{bmatrix} \rho \boldsymbol{u} \cdot \boldsymbol{n} \\ (\rho \boldsymbol{u} \cdot \boldsymbol{n}) \, \boldsymbol{u} + P \boldsymbol{n} \\ (\boldsymbol{u} \cdot \boldsymbol{n}) \, (E + P) \end{bmatrix}.$$

Note that $\boldsymbol{u} = [u, v]^t$, where $u = \boldsymbol{u} \cdot \boldsymbol{n}$ is the normal velocity and $v = \boldsymbol{u} \cdot \boldsymbol{\tau}$ is the tangential velocity.

The discrete conservative variable is $\mathbf{W}_i^n = [\rho_i^n, \rho_i^n u_i^n, \rho_i^n v_i^n, E_i^n]^t$ and so the corresponding mirror state is $\widehat{\mathbf{W}}_i^n = [\rho_i^n, -\rho_i^n u_i^n, \rho_i^n v_i^n, E_i^n]^t$. Two possible cases may appear:

- a double symmetric rarefaction wave if $\mathbf{u}_i^n \cdot \boldsymbol{n} \leq 0$,
- a double symmetric shock wave if $\mathbf{u}_i^n \cdot \boldsymbol{n} > 0$.

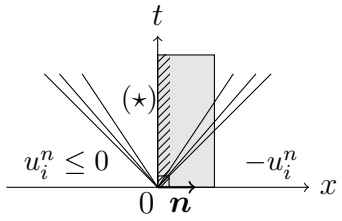

Figure B.26: Double symmetric rarefaction with mirror state in the immersed obstacle.

Appendix B.1. Double symmetric rarefaction wave: $\mathbf{u}_i^n \cdot \boldsymbol{n} \leq 0$

The computation of the wall state, classically called intermediate state $(\star)$ (see Figure B.26), is based on the symmetry of the problem, implying:

$$u^\star = 0, \tag{B.3}$$

and on the conservation of three Riemann invariants of the 1-wave:

$$\begin{cases} v^\star = v_i^n, & \text{(B.4a)} \\ s(P^\star, \rho^\star) = s(P_i^n, \rho_i^n) = s_i^n, & \text{(B.4b)} \\ u^\star + \displaystyle\int_0^{\rho^\star} \frac{c(\rho, s_i^n)}{\rho} d\rho = u_i^n + \int_0^{\rho_i^n} \frac{c(\rho, s_i^n)}{\rho} d\rho. & \text{(B.4c)} \end{cases}$$

We deduce from Equations (B.3) and (B.4c) that: $\displaystyle\int_{\rho^\star}^{\rho_i^n} \frac{c(\rho, s_i^n)}{\rho} d\rho = -u_i^n \geq 0$, allowing to retrieve the density $\rho^\star \leq \rho_i^n$ of the intermediate state, and then the pressure $P^\star$ using Equation (B.4b), such that:

$$P^\star = P_i^n \left(1 + f\left(\frac{u_i^n}{c_i^n}\right)\right).$$

The expression of the function f depends on the thermodynamic law of the fluid, but for any EOS:

$$f(0) = 0 \quad \text{and} \quad f(\xi < 0) < 0, \text{ where } \xi = \frac{u_i^n}{c_i^n}.$$

Appendix B.1.1. Ideal gas EOS

For an ideal gas such that $\rho\epsilon = \frac{P}{\gamma - 1}$, with $\gamma > 1$ the heat capacity ratio:

$$\int_{\rho^\star}^{\rho_i^n} \frac{c(\rho, s_i^n)}{\rho} d\rho = \frac{2}{\gamma - 1}(c_i^n - c^\star) = -u_i^n \quad \text{and} \quad \frac{P^\star}{P_i^n} = \left(\frac{\rho^\star}{\rho_i^n}\right)^\gamma = \left(\frac{c^\star}{c_i^n}\right)^{\frac{2\gamma}{\gamma-1}}$$

$$\Rightarrow \begin{cases} P^\star = P_i^n \left(1 + \dfrac{\gamma - 1}{2} \dfrac{u_i^n}{c_i^n}\right)^{\frac{2\gamma}{\gamma-1}} & \text{if } -\frac{2}{\gamma-1} < \frac{u_i^n}{c_i^n} \leq 0, \\ P^\star = 0 & \text{otherwise.} \end{cases}$$

Appendix B.1.2. Stiffened gas EOS

For a stiffened gas such that $\rho\epsilon = \frac{P+\gamma\Pi_\infty}{\gamma-1}$, with $\Pi_\infty \geq 0$ the reference pressure:

$$\int_{\rho^\star}^{\rho_i^n} \frac{c(\rho, s_i^n)}{\rho} d\rho = \frac{2}{\gamma-1}(c_i^n - c^\star) = -u_i^n \quad \text{and} \quad \frac{P^\star + \Pi_\infty}{P_i^n + \Pi_\infty} = \left(\frac{\rho^\star}{\rho_i^n}\right)^\gamma = \left(\frac{c^\star}{c_i^n}\right)^{\frac{2\gamma}{\gamma-1}}$$

$$\Rightarrow \begin{cases} P^\star + \Pi_\infty = (P_i^n + \Pi_\infty)\left(1 + \dfrac{\gamma-1}{2}\dfrac{u_i^n}{c_i^n}\right)^{\frac{2\gamma}{\gamma-1}} & \text{if } -\frac{2}{\gamma-1} < \frac{u_i^n}{c_i^n} \leq 0, \\ P^\star = -\Pi_\infty & \text{otherwise.} \end{cases}$$

Appendix B.1.3. First order expansion of the function f for any EOS

For all $\xi \in \mathbb{R}^-$, the function $f(\xi)$ and its derivative $f'(\xi)$ are evaluated in the neighbourhood of zero in order to get a first order expansion for any EOS.

Noting $f(\xi) = \dfrac{P^\star - P_i^n}{P_i^n}(\xi)$, and using the mean value theorem and Equation (B.4b), $\widetilde{\rho} \in [\rho^\star, \rho_i^n]$ exists such that:

$$P^\star - P_i^n = \widetilde{\partial_\rho P|_s}\,(\rho^\star - \rho_i^n)\,.$$

Moreover Equation (B.4c) suggests that $\widehat{\rho} \in (\rho^\star, \rho_i^n)$ exists such that:

$$u_i^n = -\int_{\rho^\star}^{\rho_i^n} \frac{c(\rho, s_i^n)}{\rho} d\rho = \frac{\widehat{c(\rho, s_i^n)}}{\rho}\,(\rho^\star - \rho_i^n)\,.$$

We conclude that:

$$f(\xi) = \frac{1}{P_i^n}\widetilde{c^2}\widehat{\frac{\rho}{c(\rho, s_i^n)}}u_i^n = \frac{c_i^n}{P_i^n}\widetilde{c^2}\widehat{\frac{\rho}{c(\rho, s_i^n)}}\xi \underset{\xi\to 0^-}{\sim} \frac{\rho_i^n\left(c_i^2\right)^n}{P_i^n}\xi,$$

since $\rho^\star \to \rho_i^{n-}$ when $\xi \to 0^-$.

Hence the function f is differentiable in $\xi = 0^-$ such that, for any EOS:

$$f(0^-) = 0 \quad \text{and} \quad f'(0^-) = \hat{\gamma}_i^n = \frac{\rho_i^n\left(c_i^2\right)^n}{P_i^n}.$$

Appendix B.2. Double symmetric shock wave: $\mathbf{u}_i^n \cdot \boldsymbol{n} > 0$

The computation of the intermediate state ($\star$) (see Figure B.27) is based on the Rankine-Hugoniot jump relations for a shock (B.5), and also on the symmetry of the problem:

$$\begin{aligned} u^\star &= 0, \\ -\sigma\,[\boldsymbol{W}]_i^\star + [\boldsymbol{F}(\boldsymbol{W})\cdot\boldsymbol{n}]_i^\star &= 0, \end{aligned} \tag{B.5}$$

where for any field Ψ, the jump is defined as: $[\Psi]_i^\star = \Psi^\star - \Psi_i^n$ and σ is the speed of the shock wave.

This system of jump relations (B.5) gives:

$$\begin{cases} [v]_i^\star = 0, & \text{(B.6a)} \\ [\epsilon]_i^\star + \dfrac{P_i + P^\star}{2}\left[\dfrac{1}{\rho}\right]_i^\star = 0, & \text{(B.6b)} \\ \rho_i\rho^\star\left([u]_i^\star\right)^2 - [P]_i^\star\,[\rho]_i^\star = 0, & \text{(B.6c)} \end{cases}$$

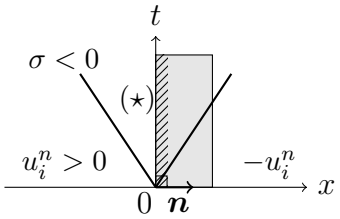

Figure B.27: Double symmetric shock with mirror state in the immersed obstacle.

which allows to determine the intermediate density $\rho^\star > \rho_i^n$ and the intermediate pressure $P^\star$. For any EOS, the pressure reads as follows:

$$P^\star = P_i^n \left(1 + g\left(\frac{u_i^n}{c_i^n}\right)\right).$$

The function g verifies:

$$g(0) = 0 \quad \text{and} \quad g(\xi > 0) > 0, \text{ where } \xi = \frac{u_i^n}{c_i^n}.$$

Appendix B.2.1. Ideal gas EOS

For an ideal gas, the solution is detailed in [25]. We get the solution of the intermediate state, writing:

$$P^\star = P_i^n \left(1 + \gamma \frac{u_i^n}{c_i^n}\left(1 + \frac{(\gamma+1)^2}{16}\left(\frac{u_i^n}{c_i^n}\right)^2\right)^{\frac{1}{2}} + \frac{\gamma(\gamma+1)}{4}\left(\frac{u_i^n}{c_i^n}\right)^2\right).$$

Appendix B.2.2. Stiffened gas EOS

For a stiffened gas, the solution of the intermediate state is:

$$P^\star + \Pi_\infty = (P_i^n + \Pi_\infty)\left(1 + \gamma \frac{u_i^n}{c_i^n}\left(1 + \frac{(\gamma+1)^2}{16}\left(\frac{u_i^n}{c_i^n}\right)^2\right)^{\frac{1}{2}} + \frac{\gamma(\gamma+1)}{4}\left(\frac{u_i^n}{c_i^n}\right)^2\right).$$

Appendix B.2.3. First order expansion of the function g for any EOS

For all $\xi \in \mathbb{R}^+$, the function $g(\xi) = \dfrac{P^\star - P_i^n}{P_i^n}(\xi)$ is evaluated to get a first order expansion for any EOS. The mean value theorem suggests that $\widetilde{\rho} \in (\rho_i^n, \rho^\star)$ and $\widetilde{\epsilon} \in (\epsilon^n, \epsilon^\star)$ exist and such that:

$$P^\star - P_i^n = \widetilde{\partial_\rho P|_\epsilon}\,(\rho^\star - \rho_i^n) + \widetilde{\partial_\epsilon P|_\rho}\,(\epsilon^\star - \epsilon^n) = a\,[\rho]_i^\star + b\,[\epsilon]_i^\star.$$

Thus Equation (B.6b) implies:

$$[P]_i^\star = \left(a + b\frac{P_i^n + P^\star}{2\rho_i^n \rho^\star}\right)[\rho]_i^\star,$$

and Equation (B.6c) gives:

$$\left([P]_i^\star\right)^2 = \rho_i^n \rho^\star \left(a + b\frac{P_i^n + P^\star}{2\rho_i^n \rho^\star}\right)(u_i^n)^2.$$

Thus, we conclude:

$$g(x) = \frac{c_i^n}{P_i^n}\left(\rho_i^n \rho^\star \left(a + b\frac{P_i^n + P^\star}{2\rho_i^n \rho^\star}\right)\right)^{\frac{1}{2}} \xi.$$

Since $\partial_\rho P|_\epsilon + \partial_\epsilon P|_\rho \frac{P}{\rho^2} = c^2$, the equivalent when $\rho^\star \to \rho_i^{n+}$ is:

$$g(x) \underset{\xi \to 0^+}{\sim} \frac{\rho_i^n \left(c_i^2\right)^n}{P_i^n}\xi.$$

Hence the function g is differentiable in $\xi = 0^+$ and such that, for any EOS:

$$g(0^+) = 0 \quad \text{and} \quad g'(0^+) = \hat{\gamma}_i^n = \frac{\rho_i^n \left(c_i^2\right)^n}{P_i^n}.$$

Property Appendix B.1. *For any EOS such that $P = \mathcal{P}(\rho, \epsilon)$, the fitting between the double symmetric shock solution and the double symmetric rarefaction solution is C^1:*

$$\forall\ \xi \in \mathbb{R},\ f(\xi) \equiv g(\xi) + o(\xi)\ \textit{when}\ \xi \to 0, \tag{B.7}$$

and the derivative value is: $f'(0) = g'(0) = \hat{\gamma}_L = \left(\frac{\rho c^2}{P}\right)_L$.

Appendix C. Analytic solution of a shock tube interaction with a wall

Appendix C.1. Initial condition: the shock tube

The analytic solution is based on the exact solution of 1D Riemann problems for the Euler equations. The calculation is performed with an ideal gas or a stiffened gas EOS. At the beginning of the computation, the shock tube apparatus contains a membrane ($x = x_0$) separating two different initial constant fluid states at rest: the right state $\boldsymbol{W}_R$ and the left state $\boldsymbol{W}_L$ (see Figure C.28). The tube is closed on the right side: $x = x_1$.

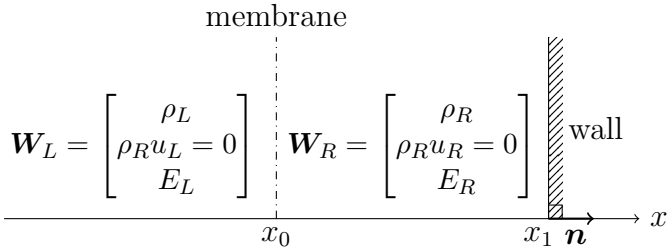

Figure C.28: Sketch of the shock tube apparatus, with the initial condition: $u_L = u_R = 0$ and $P_L > P_R$.

The solution of this Riemann problem can be computed using [28] in order to evaluate the two intermediate states $\boldsymbol{W}_1$ and $\boldsymbol{W}_2$ respectively on the left and the right side of the contact discontinuity travelling at speed $u_1 = u_2 > 0$. Since $u_L = u_R = 0$ and $P_L > P_R$, the unique solution is a 1-rarefaction wave that propagates towards the left side, and a 3-shock wave travelling at the celerity σ_2 that moves to the right. We assume in addition that the initial pressure ratio P_L/P_R is such that $u_1 - c_1 < 0$.

Appendix C.2. Shock wave reflection with the wall for an ideal gas

The shock wave generated by the shock tube hits the wall in $x = x_1$ at time $t = t_0$ (see Figure C.29):

$$t_0 = \frac{x_1 - x_0}{\sigma_2},$$

where σ_2 is the celerity of the 3-shock wave. In order to evaluate the state $\boldsymbol{W}_3$, we need to calculate the Riemann problem for $t > t_0$ with the initial condition (see Figure C.30):

$$\begin{cases} \boldsymbol{W}(x < x_1, t = t_0) = \boldsymbol{W}_2 = [\rho_2, \rho_2 u_2, E_2]^t, \\ \boldsymbol{W}(x > x_1, t = t_0) = \widehat{\boldsymbol{W}}_2 = [\rho_2, -\rho_2 u_2, E_2]^t, \end{cases}$$

with $u_2 > 0$, obtained above by solving the shock tube Riemann problem.

This 1D Riemann problem is solved with the primitive variables: $\boldsymbol{Z}_2 = [\rho_2, u_2, P_2]^t$ and $\widehat{\boldsymbol{Z}}_2 = [\rho_2, -u_2, P_2]^t$. The new intermediate state (3) (see Figure C.29) with $\boldsymbol{Z}_3 = [\rho_3, u_3, P_3]^t$ is the reflected shock wave on the wall. The Rankine-Hugoniot jump relations of the Euler equations and the symmetry of the problem give:

$$\begin{cases} u_3 = 0, \\ [\epsilon]_2^3 + \dfrac{P_2 + P_3}{2} \left[\dfrac{1}{\rho}\right]_2^3 = 0, \\ \rho_2 \rho_3 \left([u]_2^3\right)^2 - [P]_2^3 [\rho]_2^3 = 0. \end{cases}$$

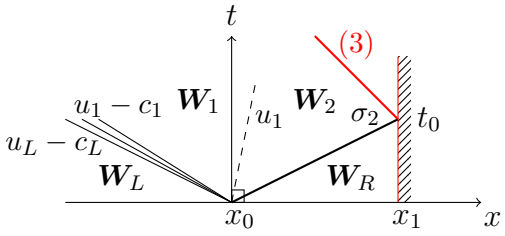

Figure C.29: Reflection of the shock wave on the wall (subsonic case: $u_1 - c_1 < 0$) at $t = t_0$.

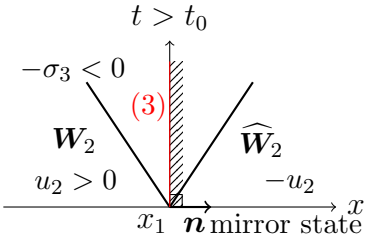

Figure C.30: Riemann problem for $t > t_0$: double symmetric shock wave with a mirror state.

For an ideal gas EOS, $P = (\gamma - 1)\rho\epsilon$, it implies the following equation with respect to $z = \dfrac{\rho_3}{\rho_2}$:

$$g(z) = \frac{(z-1)^2}{z(\beta - z)} = \frac{1}{\beta + 1}\frac{\rho_2 u_2^2}{P_2} := b, \tag{C.3}$$

using the standard notation $\beta = \frac{\gamma+1}{\gamma-1} > 1$. There exists a unique solution $z_0 \in [1, \beta)$ of Equation (C.3):

$$z_0 = \frac{2 + b\beta + \sqrt{\Delta}}{2(1+b)}, \tag{C.4}$$

with the positive discriminant $\Delta = b\beta\left(b\beta + 4\left(1 - \frac{1}{\beta}\right)\right)$.
The state $\boldsymbol{Z}_3 = [\rho_3, u_3, P_3]^t$ is thus known.

Appendix C.3. Interaction of the contact discontinuity with the reflected shock wave for an ideal gas

The initial contact discontinuity created by the shock tube interacts with the reflected shock wave in $x = x^*$ at the time $t = t_1$ (see Figure C.31), such that:

$$(u_1 + \sigma_3)t_1 = x_1 - x_0 + \sigma_3 t_0, \tag{C.5}$$

with $\sigma_3 > 0$.

For $t > t_1$, there exists a unique solution of the Riemann problem since the initial condition:

$$\begin{cases} \boldsymbol{W}(x < x^*, t = t_1) = \boldsymbol{W}_1, \\ \boldsymbol{W}(x > x^*, t = t_1) = \boldsymbol{W}_3, \end{cases}$$

is such that: $u_3 - u_1 = -u_1 < 0 < \frac{2}{\gamma-1}(c_1 + c_3)$. Since $u_1 > u_3 = 0$ and $P_1 = P_2 < P_3$ (pressure increases through a shock), the unique solution of this Riemann solution cannot involve a 1-rarefaction wave. The solutions can be either:

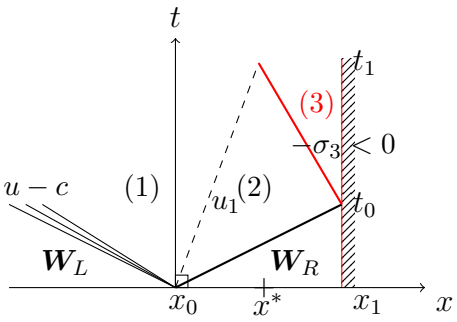

Figure C.31: Interaction of the reflected shock wave with the initial contact discontinuity (subsonic case: $u_1 - c_1 < 0$).

1. a 1-shock / 3-rarefaction configuration,
2. a 1-shock / 3-shock configuration.

Appendix C.3.1. 1-Shock / 3-rarefaction solution

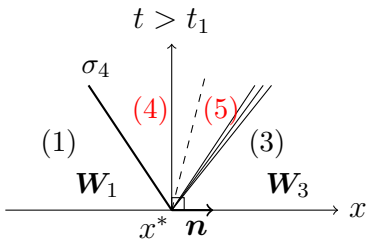

Figure C.32: Riemann problem: 1-shock / 3-rarefaction.

We wish to compute intermediate states $\boldsymbol{W}_4$ and $\boldsymbol{W}_5$ (see Figure C.32). We recall that we have $u_3 = 0$ and $P_3 > P_1$. Moreover the unknowns are such that $u_4 = u_5$ and $P_4 = P_5$. The jump relations for the 1-shock yield:

$$\begin{cases} (u_1 - u_4)^2 = (P_1 - P_4)(\tau_4 - \tau_1), \\ \mu_1 = \dfrac{P_4}{P_1} = \dfrac{\beta z_1 - 1}{\beta - z_1} > 1, \end{cases}$$

with $z_1 = \dfrac{\rho_4}{\rho_1} = \dfrac{\tau_1}{\tau_4} > 1$, $\tau = \frac{1}{\rho}$ is the specific volume. We derive:

$$z_1 = \frac{1 + \beta\mu_1}{\beta + \mu_1} \quad \text{and} \quad u_1 - u_4 = \sqrt{\tau_1 P_1}\sqrt{\beta - 1}\,(\mu_1 - 1)\,\frac{1}{\sqrt{1 + \beta\mu_1}}.$$

The Riemann invariants of the 3-rarefaction are:

$$\begin{cases} u_3 - \dfrac{2}{\gamma - 1}c_3 = u_5 - \dfrac{2}{\gamma - 1}c_5 \quad \text{with} \quad c = \sqrt{\gamma P \tau}, \\ s_3(P_3, \tau_3) = s_5(P_5, \tau_5) \Rightarrow P_3 \tau_3^\gamma = P_5 \tau_5^\gamma. \end{cases}$$

The whole set of relations implies:

$$u_4 = u_5 = u_5 - u_3 = \frac{2}{\gamma - 1} c_3 \left(\mu_2^{\frac{\gamma-1}{2\gamma}} - 1 \right) \leq 0,$$

since the 3-wave is a rarefaction wave, so $\mu_2 = \frac{P_5}{P_3} \leq 1$. The final scalar equation with respect to μ_1 that needs to be solved is:

$$l(\mu_1) = u_1 - u_3 = u_1,$$

where the function l is defined by $l(\mu_1) = A_1 \frac{\mu_1 - 1}{\sqrt{1+\beta\mu_1}} + \frac{2}{\gamma-1} c_3 \left(\left(\frac{\mu_1}{a} \right)^{\frac{\gamma-1}{2\gamma}} - 1 \right)$, with:

$$A_1 = \sqrt{\tau_1 P_1} \sqrt{\beta - 1} \quad \text{and} \quad a = \frac{P_3}{P_1} \geq 1.$$

We remark that $\frac{\mu_1}{\mu_2} = a$, since $P_5 = P_4$.
In the current wave configuration, $\mu_1 \in (1, a]$, since $\mu_1 = \frac{P_4}{P_1} > 1$ and $\mu_2 = \frac{\mu_1}{a} \leq 1$ thus $\mu_1 \leq a$. The function $l(\mu_1)$ is strictly increasing over the interval $(1, a]$ from $l(1) < 0$ to $l(a) > 0$. Thus, if $u_1 \in (0, l(a)]$, the unique solution is the present configuration with a 1-shock / 3-rarefaction configuration, else, if $u_1 > l(a)$, the solution is the 1-shock / 3-shock configuration as detailed below.

Appendix C.3.2. 1-Shock / 3-shock solution

The jump relations for the 3-shock give:

$$\begin{cases} (u_5 - u_3)^2 = (u_4 - u_3)^2 = (P_5 - P_3)(\tau_3 - \tau_5), \\ \mu_2 = \dfrac{P_5}{P_3} = \dfrac{\beta z_2 - 1}{\beta - z_2} > 1. \end{cases}$$

Similarly, it follows $z_2 = \dfrac{1 + \beta\mu_2}{\beta + \mu_2}$. So the scalar non-linear equation to be solved for the 1-shock / 3-shock configuration is:

$$q(\mu_2) = A_1 \frac{a\mu_2 - 1}{\sqrt{1 + a\beta\mu_2}} + A_2 \frac{\mu_2 - 1}{\sqrt{1 + \beta\mu_2}} = u_1 - u_3 = u_1,$$

with $A_2 = \sqrt{\tau_3 P_3} \sqrt{\beta - 1}$ and $\mu_2 = \dfrac{P_5}{P_3} > 1$.
This equation has a unique solution if and only if $u_1 > A_1 \dfrac{a - 1}{\sqrt{1 + a\beta}}$.

Hence, two configurations are identified:

- if $u_1 > A_1 \dfrac{(a-1)}{\sqrt{1+a\beta}}$ the solution is the 1-shock–3-shock configuration with $\mu_2 > 1$ such that $q(\mu_2) = u_1$,
- if $0 < u_1 \leq A_1 \dfrac{(a-1)}{\sqrt{1+a\beta}}$, the solution is the 1-shock–3-rarefaction configuration with $\mu_1 \in [1, a]$ such that $l(\mu_1) = u_1$.

This completely determines states $\boldsymbol{W}_4$ and $\boldsymbol{W}_5$.

Appendix C.4. Shock wave reflection with the wall for a stiffened gas EOS

The calculation of the analytic solution is now performed with a stiffened gas thermodynamic law.

The method of calculation is the same as with an ideal gas EOS. A 1D Riemann problem is solved, thanks to the jump relations. For a stiffened gas, the EOS is:

$$P + \gamma\Pi_\infty = (\gamma - 1)\rho\epsilon.$$

This implies:

$$c^2 = \gamma(P + \Pi_\infty)\tau \quad \text{and} \quad s = (P + \Pi_\infty)\tau^\gamma.$$

The jump relations for a 1-shock and the symmetry of the problem give:

$$\begin{cases} u_3 = 0, & \text{(C.10a)} \\ \left([u]_2^3\right)^2 + [P + \Pi_\infty]_2^3 [\tau]_2^3 = 0, & \text{(C.10b)} \\ [\epsilon]_2^3 + \dfrac{P_2 + P_3}{2} [\tau]_2^3 = 0. & \text{(C.10c)} \end{cases}$$

Equation (C.10c) is equivalent to:

$$[\tau(P + \Pi_\infty)]_2^3 + (\gamma - 1)\frac{P_2 + \Pi_\infty + P_3 + \Pi_\infty}{2} [\tau]_2^3 = 0.$$

The change of variable $\widetilde{P} = P + \Pi_\infty$ thus yields:

$$\begin{cases} \left([u]_2^3\right)^2 + \left[\widetilde{P}\right]_2^3 [\tau]_2^3 = 0, \\ \dfrac{\tau_2 + \tau_3}{2} \left[\widetilde{P}\right]_2^3 + \gamma \dfrac{\widetilde{P}_2 + \widetilde{P}_3}{2} [\tau]_2^3 = 0. \end{cases}$$

The same system than for the ideal gas EOS is recovered. The solution is then identical. The unknown is always the ratio $z = \frac{\rho_3}{\rho_2}$ and the equation to be solved is:

$$g(z) = \frac{(z-1)^2}{z(\beta - z)} = \frac{\gamma - 1}{2\gamma} \frac{\rho_2 u_2^2}{\widetilde{P}_2} := b.$$

The unique solution of this equation is called $z_0 > 1$ and the relation $\dfrac{P_3 + \Pi_\infty}{P_2 + \Pi_\infty} = \dfrac{\beta z_0 - 1}{\beta - z_0}$ allows to retrieve the pressure variable:

$$P_3 - P_2 = (P_2 + \Pi_\infty)(\beta + 1)\frac{z_0 - 1}{\beta - z_0}.$$

Remark Appendix C.1 (low velocity situation). *In the case of low Mach number, $b \ll 1$, then a first order approximation of the solution is:*

$$z_0 \approx 1 + \sqrt{b(\beta - 1)},$$

thus $P_3 - P_2 = (P_2 + \Pi_\infty)\,\gamma \dfrac{|u_2|}{c_2}$ and if $P_2 \ll \Pi_\infty$, the relative difference is close to $\dfrac{P_3 - P_2}{P_2} \approx \gamma \dfrac{\Pi_\infty}{P_2} \dfrac{|u_2|}{c_2}$.

References

[1] Nuclear Energy Agency (NEA), Loss-Of-Coolant Accident (LOCA). https://www.oecd-nea.org/nsd/reports/2009/nea6846_LOCA.pdf, 2009.

[2] Institut de Radioprotection et de Sûreté Nucléaire (IRSN), Reactivity-Initiated Accident (RIA). https://www.irsn.fr/FR/connaissances/Installations_nucleaires/Les-centrales-nucleaires/criteres_surete_ria_aprp/Pages/1-accident-reactivite-RIA.aspx, September 2018.

[3] F. Barre and M. Bernard. The CATHARE code strategy and assessment. *Nuclear Engineering and Design*, 124(3):257-284, 1990.

[4] EDF R&D, https://code-saturne.org/cms/sites/default/files/docs/5.2/theory.pdf. *Code_Saturne 5.2.0 Theory Guide*, March 2018.

[5] S. Aubry, C. Caremoli, J. Olive, and P. Rascle. The THYC three-dimensional thermal-hydraulic code for rod bundles: recent developments and validation tests. *Nuclear technology*, 112(3):331–345, 1995.

[6] I. Toumi, A. Bergeron, D. Gallo, E. Royer, and D. Caruge. FLICA-4: A three-dimensional two-phase flow computer code with advanced numerical methods for nuclear applications. *Nuclear Engineering and Design*, 200:139–155, 2000.

[7] M. Grandotto and P. Obry. Steam generators two phase flows numerical simulation with liquid and gas momentum equations. *Nuclear Science and Engineering*, 151:313–318, 2005.

[8] M. Grandotto and P. Obry. Calculs des écoulements diphasiques dans les échangeurs par une méthode aux éléments finis. *Revue Européenne des Eléments Finis*, 5(1):53–74, 1996.

[9] M. Belliard. *Méthodes de décomposition de domaine et de frontière immergée pour la simulation des composants nucléaires*. Habilitation à diriger des recherches, Aix-Marseille Université, https://tel.archives-ouvertes.fr/tel-01085328, 2014.

[10] GEXCON, https://www.gexcon.com/products-services/FLACS-Software/22/en. *FLACS Software*, January 2018.

[11] Y. Davit, C.G. Bell, H.M. Byrne, L.A.C. Chapman, L.S. Kimpton, K.H.L. Lang, G.E. Leonard, J.M. Oliver, N.C. Pearson, R.J. Shipley, S.L. Waters, J.P. Whiteley, B.D. Wood, and M. Quintard. Homogenization via formal multiscale asymptotics and volume averaging: how do the two techniques compare? *Advances in Water Resources*, 62:178–206, 2013.

[12] L. Girault and J.-M. Hérard. Multidimensional computations of a two-fluid hyperbolic model in a porous medium. *International Journal on Finite Volumes*, 7(1):1–33, https://hal.archives-ouvertes.fr/hal-01114209, September 2010.

[13] R. Eymard, T. Gallouët, and R. Herbin. Finite Volume Methods. *Handbook for Numerical Analysis, P.G. Ciarlet, J.L. Lions eds, North Holland*, 7:713–1020, October 2006.

[14] A.-J. Chorin. Numerical solution of the Navier-Stokes equations. *Mathematics of Computation*, 22(104):745–762, 1968.

[15] R. Temam. Sur l'approximation de la solution des équations de Navier-Stokes par la méthode des pas fractionnaires (II). *Archive for Rational Mechanics and Analysis*, 33(5):377–385, January 1969.

[16] D.-R. Van Der Heul, C. Vuik, and P. Wesseling. A conservative pressure-correction method for flow at all speeds. *Computers & Fluids*, 32:1113–1132, 2003.

[17] T. Gallouët, L. Gastaldo, J.-C. Latché, and R. Herbin. An unconditionnally stable pressure correction scheme for compressible barotropic Navier-Stokes equations. *ESAIM: Mathematical Modelling and Numerical Analysis*, 44(2):251–287, 2010.

[18] W. Kheriji, R. Herbin, and J.-C. Latché. Pressure correction staggered schemes for barotropic one-phase and two-phase flows. *Computers & Fluids*, 88:524–542, 2013.

[19] C. Zaza. *Contribution to numerical methods for all Mach flow regimes and to fluid-porous coupling for the simulation of homogeneous two-phase flows in nuclear reactors*. PhD thesis, Aix-Marseille Université, https://tel.archives-ouvertes.fr/tel-01135355, 2015.

[20] F. Archambeau, J.-M. Hérard, and J. Laviéville. Comparative study of pressure-correction and Godunov-type schemes on unsteady compressible cases. *Computers & Fluids*, 38:1495–1509, 2009.

[21] J.-M. Hérard and X. Martin. An integral approach to compute compressible fluid flows in domains containing obstacles. *International Journal on Finite Volumes*, 12(1):1–39, https://hal.archives-ouvertes.fr/hal-01166478, December 2015.

[22] R. Menikoff and B.J. Plohr. The Riemann problem for fluid flow of real materials. *Rev. Mod. Phy.*, 61(1):75–130, 1989.

[23] X. Martin. *Modélisation d'écoulements fluides en milieu encombré d'obstacles.* PhD thesis, Aix-Marseille Université, Chapter 3, pages 207–238, https://tel.archives-ouvertes.fr/tel-01235089, 2015.

[24] R. Eymard, T. Gallouët, C. Guichard, R. Herbin, and R. Masson. TP or not TP, that is the question. *Computational Geosciences*, 18:285–296, August 2014.

[25] T. Buffard, T. Gallouët, and J.-M. Hérard. A sequel to a rough Godunov scheme: application to real gases. *Computers & Fluids*, 29:13–847, 2000.

[26] F. Dubois. Boundary conditions and the Osher scheme for the Euler equations of gas dynamics. *Internal Report CMAP 170, Ecole Polytechnique, Palaiseau, France*, 1987.

[27] F. Blondel, B. Audebert, T. Pasutto, and M. Stanciu. Condensation models and boundary conditions for non-equilibrium wet steam flows. *International Journal on Finite Volumes*, 10:1–53, June 2013.

[28] J. Smoller. *Shock Waves and Reaction-Diffusion Equations*, volume 258 of *A Series of Comprehensive Studies in Mathematics*. Springer-Verlag, New York, 1994.